RAM ROBOTICS AND MECHATRONICS

AERODYNAMIC MODELING OF FLAPPING-WING UAV'S IN THE PORT HAMILTONIAN FRAMEWORK

M.T.E. (Mohab) Abdelbadie

MSC ASSIGNMENT

Committee:
prof. dr. ir. S. Stramigioli
dr. ir. R.A.M. Rashad Hashem
dr. ir. F. Califano
dr. L.D. De Santana

April, 2021

025RaM2021
Robotics and Mechatronics
EEMathCS
University of Twente
P.O. Box 217
7500 AE Enschede
The Netherlands

UNIVERSITY OF TWENTE. | TECHMED CENTRE
UNIVERSITY OF TWENTE. | DIGITAL SOCIETY INSTITUTE

Aerodynamic Modeling of Flapping-wing UAVs in the Port Hamiltonian Framework

<Mohab Tarek Elsayed Abdelbadie>

April 29, 2021

Acknowledgments

First, I would like to show my gratitude to my daily supervisor and my teacher Ramy Rashad. Ramy has always been a great support and I am sure that this thesis wouldn't have come to an end without him. I would like to thank Ramy for always comforting me at the most stressful times of this thesis especially during the lockdown. I would like to thank him for his positive criticism and his detailed feedback that covers every single detail. last but not least, I would like to thank him for always making extra time for more discussions.

Next in line is my second daily supervisor Federico Califano. I am so thankful for having him as one of my supervisors. His continuous criticism and notes were always important and pushing forward. I would like to thank Federico for his interest in joining our project from the first place and also for making extra time for more comments. I wish to express my sincere appreciation to both Federico and Ramy for teaching me how to conduct an objective scientific research.

I would like to thank my best friend in Enschede, Jelle Bijlsma. I would like to thank him for his continuous support and motivation during the thesis period. I also like to thank him for his valuable comments on my manuscript and for spending much time giving feedback on rehearsing for the final presentation. I would like to show my appreciation for always being there when I need him and being a true friend.

Last but not least, I wish to show my gratitude to my roommates, Sjoerd, Eliana and Mihaela. I would not have been able to make it in Enschede during the lockdown if I didn't have such supportive and caring roommates. I like to thank them for always pushing me forward and motivating me on my hardest times.

Finally, I would like to thank my close friend Nour Magdy for always supporting and believing in me. I would like to thank her for being there during my hardest times.

In conclusion, people who are close to me know how stressing and draining this period was, especially due to the lockdown and working from home. If it wasn't for the support of these people, I would have never made it till the end. Thank you all so much.

Abstract

Recently, Flapping-wing UAVs have been used in different applications. For example, in airports, birds tend to collide with aeroplanes during their take off and landing causing damage to the planes and death to the birds. One way to solve this is to use bird-like robots to scare these birds away and prevent collision. To have an ornithopter that can be controlled to do this, a dynamic model has to be developed. Since flapping ornithopters are physical systems which are governed by energy, the focus of this thesis is to develop a full dynamic model in an energy-based manner. This work provides a systematic way of rigid-body modeling in the Port Hamiltonian framework based on the work of (27). The procedure is applied on a multi-body flapping-wing UAV. The final port Hamiltonian model is an open model that can be connected to other sub-systems such as the air and a controller sub-system. The connection between the preliminary model and the air resembles the aerodynamic contribution on the flapping-wing UAV, which is the second contribution of this work.

Flapping flight is a highly complicated mechanism exhibiting unsteady behaviour. Scientists throughout the last century and till now have been studying the physics behind flying animals. They adopted aerodynamic models to predict their behaviour. In majority of literature, they developed quasi-steady assumptions. These models ignore the unsteady wake effects and do not capture most of the unsteady phenomena of flapping. This thesis focuses on a realistic, unsteady aerodynamic model that takes into account most of the unsteady phenomenon of flapping. The model adopted in this work is the model by Delaurier (8) in 1993. The aerodynamic model is connected to the port Hamiltonian dynamic model of flapping-wing UAVs. The model was validated and proven to be working through a set of four experiments. The first experiment is a time history to predict the generated aerodynamic forces. The other three experiments are sweeping over different flight parameters such as the pitch angle of the bird θ_a, flight speed U and flapping frequency f. An optimal value of flapping frequency $f = 2.9Hz$ that maximizes the thrust and generates positive lift, was observed through the fourth experiment. Interestingly, this value agrees with previous work that was performed on a similar model, the Robird. In conclusion, this thesis provide a full dynamic model in the port Hamiltonian framework, that can be used as a plant for future control purposes.

Contents

1 Introduction

For more than a century now, biologists and applied mathematicians started studying the science behind flying animals. In order to design and build bird-like machines that have the capability of flying, scientists should have a deep knowledge of the mechanisms birds use to achieve flying. Flying animals with flapping wings such as birds and insects utilize different flight mechanisms to generate enough lift and thrust to overcome their weight and be able to fly. Unlike fixed-wing aircrafts, flapping-wing aerial vehicles do not have an additional propulsive source of thrust. Due to air flow around the wings, they are able to generate lift and thrust by flapping their wings. So in order to study flapping flight aerodynamics, scientists had to study the complicated relation between the air near the flapping wings and the generated output forces. They adopted aerodynamic models to study this behaviour. In flapping flight, steady assumptions of the flow are no longer valid as they hide most of the flow properties. Thus, aerodynamics of flapping-wing UAVs has always been a more complicated problem compared to fixed-wing (or rotary-wing) UAVs.

The first attempts of explaining the physics behind animals' flight were conducted in the beginning of the 20th century by Knoller in 1909 and Betz in 1912 (37). Later, in the second half of the 20th century, the research intensified more and scientists started to grasp the necessary knowledge for simulating animals' flight on machines. In the next section of this chapter, a summary of the research regarding the aerodynamic modeling of flapping wing vehicles is shown.

1.1 Aerodynamic Modeling

This section gives a glimpse about the main contributions concerning aerodynamic modeling in the late 20th century. To have a good grasp of the basics of aerodynamic modeling of flapping wing animals, six prevailing methods were used (14):

1. Momentum Theory
2. Blade Element Theory
3. Hybrid Momentum Theory
4. Lifting Line Method
5. Lifting Surface Method
6. Two Dimensional Thin Airfoil theory

In this section, a shorted explanation of these methods is given alongside with their limitations. For each method, a table will be added highlighting the main contribution in flapping flight based on this theory.

1.1.1 Momentum Theory

In early 20th century, scientists started to use this simple theory for aerodynamic modeling of insects, especially for hovering. This theory relies on the three laws of conservation: conservation of mass, momentum and energy.

Limitations

An assumption of the flow being in-viscid is made, this eases the complications, however, limits the performance of the model. Another major limitation of this theory is that it does not take into account the wing characteristics such as the aspect ratio, wing area or the section's geometry. So, any changes in these parameters will not have a reflection on the output forces. As Wilkin and Williams said, this method is only aple to determins the gross values of the aerodynamic forces and the power requirements (31).

1.1.2 Blade Element Theory

This method solved the drawbacks of the momentum theory by taking into account airfoil characteristics. This is done by dividing the wing into a number of chord-wise transverse sections for which the generated aerodynamic forces can be calculated. Each section is analyzed individually and by integrating all over the whole sections of the wing, the aerodynamic forces and moments are computed. For each section, the relative wing velocity is the sum of forward, flapping and induced velocities (31). Its worth mentioning that this method was applied first on rotary wings then it was adopted for flapping wings as well. In 1980, Ellington developed actuator disk model to calculate the induced velocity of the flapping wing (10). Figure 1.1 shows a blade element theory applied to a root-flapping wing.

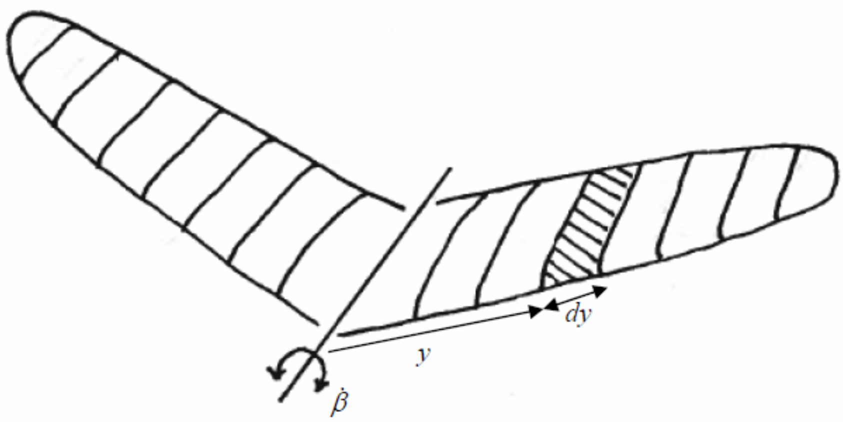

Figure 1.1: Blade element theory is applied by dividing the wing chord-wise into 8 sections (14)

1.1.3 Hybrid Momentum Theory

As the name suggests, this approach combines both the momentum with the blade element theory to reach an adequate aerodynamic model. Its also known as the vortex theory. Many pioneers of flapping wing aerodynamics including Ellington, Rayner, and Spedding have developed this theory in late 90's (10; 28; 32). The following table shows the major contributions in the 20th century based on the Hybrid momentum theory.

Year	Author	Contribution
1979	Rayner	Performed a much more detailed analysis of the wake (28),(29).
1980	Ellington	Developed a vortex theory of flight using a pulsed actuator disk to mimic the periodic beating of the flapping wings(10).
1981	Kawachi	Developed a local circulation method in the analysis of helicopter rotors and wind turbines (20).
1985	Azuma et al	Applied the method developed by Kawachi on forward flight of dragonflies (3).

1985, 1988	Azuma et al	combined blade element theory along with a more detailed analysis on the unsteady wake effects (3),(4).

Table 1.1: Major contributions based on the Hybrid momentum theory

1.1.4 Lifting Line and Lifting surface Methods

Lifting Line method

In an attempt to have a more accurate model, modifications of the above methods are required. The lifting line theory was expressed early by Frederick W. Lanchester in 1907, and by Ludwig Prandtl in 1918–1919 after working with Albert Betz and Max Munk (2). In this model, the bound vortex loses strength along the whole wingspan because it is shed as a vortex-sheet from the trailing edge, rather than just as a single vortex from the wing-tips.

year	Author	Contribution
1974	Betteridge and Archer	Implemented A method for the analysis of flapping-wing flight using lifting-line theory and actuator disc theory is proposed for the prediction of aerodynamic loads, propulsive efficiencies and optimum lift distributions (6).
1981	Philips et al	Implemented the lifting line approach in aerodynamic modeling of bird flight where near and far wakes are modeled. However, the convection of the wake was neglected (25).
1986	Ahmadi and Widnall	Developed a low frequency unsteady lifting-line method for a harmonically oscillating wing of large aspect ratio, using matched asymptotic expansions (1).
1991	Guermond and Sellier	Extended the above method to free the constraints on the reduced frequency. The method was also applied to swept wings (13).

Table 1.2: Major Contributions based on the Lifting line approach

Limitations

Lifting line theory does not take into account viscous, unsteady flow or wings with low aspect ratio. So the detailed geometric and kinematic effects of the wings are suppressed.

Lifting Surface Method

Lifting Surface method solves the above mentioned problem of the lifting line theory by permitting a more detailed representation of the wake and wing Geometry. But still, it failed to capture unsteady flow properties due to flapping.

1.1.5 Two Dimensional Thin Airfoil theory

Thin Air foil theory was widely used for fixed wing aerial vehicles. Thin airfoil theory applies a vortex sheet to a two dimensional airfoils chord line to determine the circulation, and therefore the lift, generated by the airfoil at a specific AOA. One of the major limitations of this theory is that its valid for small angles of attack.

With taking into account unsteady phenomenon of flapping flight, this theory is proven to provide an adequate aerodynamic model for flapping wings as well. In 1993, De Laurier came up with a design-oreinted aerodynamic model that does not assume quasi-steady assumptions but rather unsteady flow (8).

The following table covers the rest of the most influential aerodynamic models developed in the last decades of the 20th century. These models along with the previous ones mentioned, sat the first foot into the science of aerodynamic modeling of flapping wings flight. Starting the twenty-first century, with the development of robots, scientists tend to do more study for control purposes. To do, they developed quasi-steady models which do not capture the unsteady phenomenon of flapping-wing flight. Quasi-steady models start with some assumptions which limit their models, such as the flapping frequency has to be low. This prevents having a strong realistic model which takes into account the unsteady behaviour of flapping. For an extensive study about different models used for flapping wings, the reader is referred to (36).

Year	Author	Aero-dynamic Method	Contribution
1979	Lan	Vortex lattice method	Developed a vortex lattice approach to the modeling of oscillating flat-plate wings. The method was applied to the study of Tandem wings (22).
1993	DeLaurier	Unsteady thin airfoil theory	Developed a modified strip theory taking vortex-wake effects into account (8) *. . . explained briefly later.*
1993	Sunada et al	Vortex lattice approach	developed a vortex lattice approach to the modelling of flat plates. The method is applied to both the analysis of splitting triangular plates and the takeoff of a butterfly (34) , (35).
1996	Wilkin and Williams	Unsteady panel method	Compared the aerodynamic forces of the unsteady panel methods applied on rigid wings with quasi-steady models (31).

Table 1.3: A timeline of the Aerodynamic models developed in the 20th Century

1.2 Motivation and Contribution

In line of the literature review done in the previous section, the main contribution of this thesis is two-fold: Dynamic modeling in the port Hamiltonian framework and Aerodynamic modeling of flapping-wing UAVs . The latter relies on implementing a realistic aerodynamic model which does not assume quasi-steady assumptions. This thesis adopts the unsteady aerodynamic model by Delaurier in 1993 (8). The model uses modified strip theory approach that takes into account these unsteady phenomena:

- Partial Edge Suction
- Post Stall Behaviour
- Unsteady vortex wake effects
- Apparent Mass Effect
- Camber and frictional drag due to viscous effects
- Downwash effect

Moreover, the use of strip theory for aerodynamic modeling is considered to be a powerful tool. It can be also applied to underwater vehicles. As Lin states in his book (23), strip theory can be seen as a conversion problem from 3D to 2D since each section (strip) is treated individually as a 2D airfoil rather than dealing with the wing as a full body. Although, he uses strip theory in the context of hydrodynamics, the motivation still holds when changing water to air. For more about strip theory and its difference between blade element theory, the reader is referred to read the book (23).

The aerodynamic model of Delaurier has been adopted for the design of many ornithopters (15). Shyy and Kamakoti started by applying this model in a computational study for flapping wing flight (19). Benedict (5) developed a C++ code for practical implementation of Delaurier model. Furthermore, the model was studied by (9) with a detailed focus on the aero-elasticity part. Moreover, the model was used twice by Zakaria et al (39), (38). First, he applied the model on different ornithopters and compared their results. Later, he used the model for simulations of The Pterosaur Replica in Forward Flight.

The focus of this work is to analyze and study Delaurier model for ornithopter flight. The model is then validated on the Robird with a change in the airfoil to Liebeck LPT 110A. The Robird a falcon-like robot designed by Clear Flight Solutions[1] to scare off birds in areas where they cause harm (11), as shown in figure 1.2. In order to get this aerodynamic model validated, a dynamic model of the Robird should be available and that is the second contribution of this thesis. Since flapping wing UAVs are physical systems which are governed by energy, the dynamic modeling is better done in an energy-based form. Port-based modeling (7) is an effective approach for modeling of multi-domain physical systems. The system is then seen as an interconnection of sub-systems through power ports, where they can exchange energy. This gives a better understanding of the whole system since it is no longer seen as a bunch of signals. Moreover, the aerodynamic contribution is also seen as an external sub-system which is connected to the flapping-wing UAV. Thus, that provides more understanding of the energy exchange between flapping wings and air flow around them. With that being said, Port Hamiltonian theory is a perfect candidate for the modeling in this way. In addition,, dynamic modeling is better described in a coordinate-free approach thats why geometric formulation of rigid body motion is adopted in this work using Screw theory and Lie groups. With that being said, in this thesis, the dynamic model is developed in the port Hamiltonian framework in a geometric manner. Thus, a port-based modeling technique along side with an unsteady aerodynamic model form the main focus of this work.

[1] https://www.thedronebird.com/ The company name changed to TheDroneBird recently

Figure 1.2: The Robird

1.3 Research Questions

Since there are two main contributions for this thesis, it raises and answers two research questions: **First:** How can a port-based modeling approach be used to model an ornithopter like the Robird? Moreover, how can the Port-Hamiltonian framework play its rule in the modeling process?

Second: Considering the fact that flapping flight is highly unsteady, how can the aerodynamics of ornithopters be modeled without assuming quasi-steady assumptions? Can we reach a strong model that captures unsteady phenomenon of flight and validate this model on the Robird?

The rest of the thesis is dedicated to answer these questions.

1.4 Report Structure

The remainder of the thesis is structured as follows: The first two chapters (excluding this one) are concerned with the first research question. **Chapter 2** covers the essential background for port-based modeling. Gentle introduction to the Port-Hamiltonian framework along side with the bond graph notation are discussed. Moreover, screw theory is explained briefly. In **Chapter 3**, rigid body modeling in the Port Hamiltonian Framework is explained first. Then, the modeling approach is applied on the Robird. Furthermore, **Chapter 4** addresses the problem of aerodynamic modeling of the Robird. An extensive study of the model developed by Delaurier is performed. Final experiments to validate the aerodynamic model are covered in **Chapter 5**. Finally, **Chapter 6** draws a conclusion about the research being done in this topic and gives recommendations to future work.

2 Background: Port-based modeling and Screw theory

For the analysis and study of physical systems, mathematical models have to be formulated. These models are then used for simulation and control purposes. Port-based modeling is an effective approach for the modeling of multi-domain physical systems. It aims at providing a unified framework for modeling in any domain; mechanical, electrical or thermal. The main strength of port-based modeling compared to traditional modeling techniques lie in the following points:

- **Physical systems are governed by energy**. In other words, energy is seen as the *lingua franca* of all physical systems. Port-based modeling allows to perceive the physical system as a set of sub-systems connected to each other by power ports. Having a look at the energy of the system and its exchange between different sub-systems gives a better understanding of the behaviour of the system. For example, a moving mass with unbounded kinetic energy implies instability of the system.
- **Power and energy are coordinate-independent.** Regardless of which frame power is expressed in, it will have the same scalar value. This implies that the energy of any subsystem will not vary by the change of the frame it is expressed in. Thus, giving an objective view at the system.
- **Control by interconnection**. Actuators do exchange energy with the system in a bidirectional way. In the same sense, a controller can be also seen as a sub-system that exchanges energy with the rest of the system. Classical control theory looks at the controller as a bunch of signals, this makes it hard to study the physical behaviour of the full system.

For a more detailed explanation of the port-based modeling, the reader is referred to (7).

With that being said, an energy-aware framework should be utilised for the port-based modeling. This is achieved through studying port-Hamiltonian theory alongside with bond graph. This chapter provides the necessary background required for the rest of the thesis. First, an introduction to the port Hamiltonian framework is given. Next, an analogy between bond graph and port Hamiltonian is shown. Finally, screw theory is used for the description of motion and dynamic of rigid bodies.

2.1 Port-Hamiltonian and Bond graph

Port-Hamiltonian theory provides a framework for modeling of physical systems using the port-based approach. It combines the classical Hamiltonian dynamics with a network structure. Thus, a physical system is modeled as interconnection between sub-systems through power ports. The simplest sub-system is a basic ideal element such as a mass or a spring. This will be explained in this chapter briefly. The port Hamiltonian framework can be applied in all physical domains, however, in this chapter, the focus will be directed towards the mechanical domain since it is the concern of this thesis.

2.1.1 Intro to Hamiltonian Mechanics

Hamiltonian formulation of mechanics is similar to the Lagrangian formulation. In fact, it originated from Euler-Lagrange equations after defining the conjugate momenta $\mathbf{p}$ and Legendre transform. For a detailed study about the history of Hamiltonian mechanics, the reader is referred to (17).

The classical canonical formulation is defined by the following set of equations governing the Hamiltonian:

$$\frac{d\mathbf{p}}{dt} = -\frac{\partial \mathcal{H}}{\partial \mathbf{q}}, \tag{2.1}$$

$$\frac{d\mathbf{q}}{dt} = \frac{\partial \mathcal{H}}{\partial \mathbf{p}}. \tag{2.2}$$

Where $\mathcal{H}$, the Hamiltonian is defined as the summation of the kinetic and potential energy present in the system. q is the generalized coordinates and p is the conjugate momenta. For a one dimensional linear moving mass, q is the position and p is the linear momentum $p = m \cdot v$. The generalized coordinates and momenta can be lumped together into a *state variable* x such that $x = [p \quad q]^\top$.

Thus, the above equations 2.1 and 2.2 are then written as:

$$\dot{x} = \begin{bmatrix} 0 & -1 \\ 1 & 0 \end{bmatrix} \partial_x \mathcal{H} = J(x)\partial_x \mathcal{H}, \tag{2.3}$$

where the skew-symmetric matrix $J(x)$ is called the internal interconnection matrix , such that $J(x) = -J^\top(x)$. The skew-symmetric property is important in the conservation of Energy. For a closed system with no dissipation of the energy, to check for energy conservation, the rate of change of the Hamiltonian $\mathcal{H}$ is then,

$$\dot{\mathcal{H}} = \langle \partial_x \mathcal{H} | \dot{x} \rangle = \partial_x^\top \mathcal{H} J(x) \partial_x \mathcal{H} = 0. \tag{2.4}$$

In case of having resistive elements and external inputs, one representation of the port Hamiltonian formulation is the so-called *input-state-output* representation defined as:

$$\dot{x} = (J(x) - R(x))\partial_x \mathcal{H} + g(x)u, \tag{2.5}$$

where u is the external input. R is a resistive structure and $g(x)$ is the interconnection between the input and the system. The output y in this case is:

$$y = g^\top(x)\partial_x \mathcal{H}. \tag{2.6}$$

Before digging deeper into the port Hamiltonian framework, we have to shed the light on the bond graph theory.

Bond graph theory was first originated in 1959 by Paynter (24). The bond graph notation can be seen as a graphical representation of the port Hamiltonian theory, where basic elements are connected to each other through *bonds* representing energy flow between them. Basic elements are connected to each other through these bonds forming sub-systems, which are then connected to each other forming the complete physical system. The resulting graph is called *bond graph.*

2.1.2 Power Ports

When talking about power ports, two important conjugate terms have to be mentioned, *flow, f* and *effort, e.* In basic mechanics, an example of the flow is the velocity of a rigid body. Similarly, the effort is the force applied on this body. Together, they form the conjugate pair with a product equals to power.

$$f \in \mathbb{R}^k, \qquad\qquad e \in \mathbb{R}^k,$$
$$e^\top f = power.$$

In 3D mechanical systems, $f \in \mathcal{F}$, where $\mathcal{F}$ is the *flow space* (finite-dimension, linear space of twists). Similarly, $e \in \mathcal{E} = \mathcal{F}^*$, where $\mathcal{E}$ is the *effort space* (finite-dimension, linear space of wrenches). Their product is then defined by pairing: $\langle e|f\rangle_{\mathcal{F}}$

For a concrete definition of the *flow* and *effort* variables:

- ***flow*** is the rate of change of the state variable x, such that $f = \dot{x}$
- ***effort*** is the change of the Hamiltonian $\boldsymbol{\mathcal{H}}$ with respect to the state variable x, thus $e = \partial_x \boldsymbol{\mathcal{H}}$

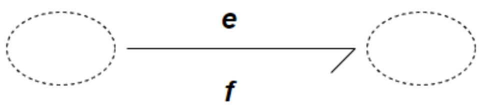

Figure 2.1: Power exchange between two elements through a power bon

In the **bond graph** notation, a power bond is represented as a straight line with a half-arrow at the end indicating direction of power flow, as shown in figure 2.1. Each bond carries two pieces of information about the effort and flow being exchanged between the two elements.

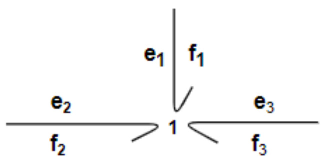

$$f_1 = f_2 = f_3$$
$$e_1 + e_2 + e_3 = 0$$

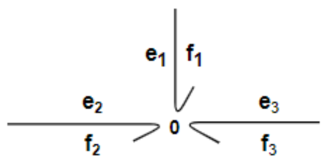

$$e_1 = e_2 = e_3$$
$$f_1 + f_2 + f_3 = 0$$

Furthermore, bonds which share the same flow are connected to each other by a **1-junction**. And bonds which have a common effort are connected to each other by a **0-junction**. Both junctions are multi-port power-conservative, which means that the sum of all power equals zero.

2.1.3 Basic Elements

As mentioned earlier, the port-based modeling approach views the physical system as interconnection between basic elements linked by energy flow. These basic elements can be categorized according to their energy behaviour into five main categories:

Energy Storage Elements

The first category is the elements which can store energy. The simplest example in the mechanical domain is: a moving mass stores kinetic energy and an elastic spring stores potential energy. In the **bond graph** notation, the moving mass is modeled as a **I-** type storage element and the spring is modeled as a **C-** type storage element.

The stroke drawn at the end of the bonds define the *causality* of the bond. The stroke aims at the direction of the effort. For example, the **I** element shown gets the effort in and flow out.

Energy Dissipation Elements

Resistive elements dissipate energy of the system, in the form of friction for example. A damper in the mechanical domain is considered as a resistive element. In the **bond graph** notation, **R-**element is used for modeling of resistive elements.

Energy Supply Elements

A port Hamiltonian system can have an external port where an external input can be connected, known as the *Interaction* port. In the **bond graph** notation, sources of flow and effort (**Sf** and **Se**) are used to impose certain flow and effort, respectively.

Both sources have fixed causality which means that a source of effort will always have its effort out and vise versa.

Energy Routing Elements

Two fundamental energy-routing elements are the transformer and the gyrator. The transformer relates flow (or effort) on one side to the flow (or effort) into the other side. The Gyrator relates the flow (effort) of one side into the effort (flow) of the other side.

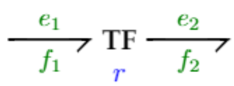

$$f_2 = r \cdot f_1$$
$$e_1 = r \cdot e_2$$

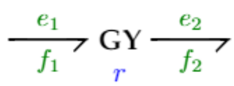

$$e_1 = r \cdot f_2$$
$$e_2 = r \cdot f_1$$

An example of the transformer is an ideal gear train with a gear ratio equals to r (in the above figure). Ideal electric motor is an example of the gyrator where the flow (current in electric domain) is converted to effort (torque).

Dirac Structure

A fundamental concept in the study of the port Hamiltonian framework is the **Dirac Structure**. The Dirac structure is a power conservative multi-port that defines energy routing and interconnection between different ports. All ports connected to a Dirac structure should have the same direction, either all inwards or all outwards, to ensure power continuity.

2.2 Screw Theory

Screw theory is used to describe motion of rigid bodies in space. This section gives a brief overview about screw theory. For a detailed explanation, the reader is referred to (33).

The configuration of a rigid body in space including pose and orientation is defined by the homogeneous matrix H where H lies in the Special Euclidean group SE(3). The configuration of a frame attached to the rigid body Ψ_a expressed in another frame Ψ_b is defined as:

$$H_a^b = \begin{pmatrix} R_a^b & \xi_a^b \\ 0_{1\times 3} & 1 \end{pmatrix}, \tag{2.7}$$

where $R_a^b \in SO(3)$, is the orthogonal rotation matrix describing the orientation of the frame Ψ_a expressed in frame Ψ_b. $xi_a^b \in \mathbb{R}^3$ is the transnational component of the body's configuration Ψ_a expressed in Ψ_b.

Screw theory uses twists and wrenches to describe rigid body motion. The Twist is the generalization of the velocity of a rigid body, expressed as a six-dimensional vector.

$$T = \begin{pmatrix} \omega \\ v \end{pmatrix}, \tag{2.8}$$

where ω is the angular velocity of the rigid body and v is the linear velocity defined as a screw motion.

The Twist of a rigid body is expressed using three indices. For example, ${}^cT_a^b$ is the twist of the frame attached to the rigid body Ψ_a with respect to Ψ_b expressed in Ψ_c. The expression for the twist is then defined by two ways as follows:

$${}^b\tilde{T}_a^b = \dot{H}_a^b H_b^a, \tag{2.9}$$

$${}^a\tilde{T}_a^b = H_b^a \dot{H}_a^b, \tag{2.10}$$

where ($\tilde{T} \in se(3)$) is defined as follows:

$$\tilde{T} = \begin{pmatrix} \tilde{\omega} & v \\ 0 & 0 \end{pmatrix}, \tag{2.11}$$

and the $tilde()$ operation is the map defined as:

$$\tilde{\omega} = \begin{pmatrix} 0 & -\omega_z & \omega_y \\ \omega_z & 0 & -\omega_x \\ -\omega_y & \omega_x & 0 \end{pmatrix}. \tag{2.12}$$

Wrenches are a generalization of the forces and torques acting on the rigid body, expressed in a six-dimensional co-vector.

$$W = \begin{pmatrix} \tau \\ f \end{pmatrix}, \tag{2.13}$$

where τ is the torques acting on the body and f is the forces affecting the body. Wrenches are dual of the Twist, when paired together, their product is the power. However, they have to be expressed in the same co-ordinate frame. Finally, wrenches are expressed using two indices, one to show the cause of the force and the other is the frame it is expressed in. For example ${}^WW_{air}$ is the wrench caused by air expressed in frame W.

3 Port Hamiltonian Modeling of the Robird

The Robird is a flapping-wing UAV that mimics a peregrine falcon. Figure 3.1 shows the Robird model and a peregine falcone side by side. One of the main applications of the Robird is to scare birds in areas where they cause harm. The Robird has two flapping wings and two movable tails connected to a base body, where a driving mechanism moves the wings back and forth to achieve flapping. The flapping mechanism it uses allows it to fly with some limitations. The goal of this chapter is to develop a dynamic model of the Robird so it can be used for control purposes. In this chapter, a dynamic model of the Robird is derived using the Port Hamiltonian Formulation. The chapter is organised as follows: First a brief explanation of the port-Hamiltonian framework for rigid body modeling is discussed. Later, the kinematics of the Robird is studied and the dynamic model of the Robird is developed.

(a) The Robird

(b) A Pergine Falcon (photo courtesy by Tze-hsin Woo) [1]

Figure 3.1: The Robird peregine falcon model versus a real peregine falcon

3.1 Rigid Body Modeling

3.1.1 Port Hamiltonian Framework

In the mechanical domain, rigid bodies can store two forms of energy, kinetic and potential energies. So, each rigid body is composed of two storage elements, one for each energy, and interaction ports to be connected to other sub-systems. It is worth mentioning that for the rest of this section, all variables will be expressed in body-fixed frame, unless mentioned otherwise.

The derivation in this section is a summary of the work of (27). For a more in-depth study of the port Hamiltonian framework for rigid body modeling, the reader is referred to (27).

Kinetic Energy

The Kinetic Energy of a body in space is defined by the Hamiltonian $\mathcal{H}_k$:

$$\mathcal{H}_k(\boldsymbol{P}) = \frac{1}{2}\boldsymbol{P}^\top \boldsymbol{\mathcal{I}}^{-1}\boldsymbol{P}, \tag{3.1}$$

where $\boldsymbol{P} \in (\mathbb{R}^6)^*$, the storage variable is the conjugate momentum to the body twist $\boldsymbol{T} \in \mathbb{R}^6$, such that $\boldsymbol{P} = \boldsymbol{\mathcal{I}}\boldsymbol{T}$. $\boldsymbol{\mathcal{I}} \in \mathbb{R}^{6\times 6}$ is the inertia tensor expressed in the body-fixed frame. When the body-fixed frame is chosen such that its origin coincides with the center of mass and the axes align with the principle axes, the inertia tensor is diagonal and corresponds to:

$$^B\boldsymbol{\mathcal{I}} = \begin{pmatrix} J^B & 0_{3\times 3} \\ 0_{3\times 3} & mI_{3\times 3} \end{pmatrix}, \tag{3.2}$$

[1] https://www.gettyimages.nl/detail/foto/peregrine-falcon-royalty-free-beeld/917064068

where m is the mass of the body and J^B is its moment of inertia around O_B expressed in Ψ_B The *effort* is the change of the **Hamiltonian** with respect to the storage variable ($\boldsymbol{P}$), $e = \partial_{\boldsymbol{P}}\boldsymbol{\mathcal{H}}_k$,

$$\partial_{\boldsymbol{P}}\boldsymbol{\mathcal{H}}_k = \boldsymbol{\mathcal{I}}^{-1}\boldsymbol{P} = \boldsymbol{T}. \tag{3.3}$$

The *flow* is the rate of change of the state variable $f = \dot{\boldsymbol{P}}$, which is the rate of change of the momentum. Using *Euler-Poincare* representation of Newton's second law with no applied force,

$$\dot{\boldsymbol{P}} = ad_{\boldsymbol{T}}^{\top}(\boldsymbol{P}) = ad_{\partial_{\boldsymbol{P}}\boldsymbol{\mathcal{H}}_k}^{\top}(\boldsymbol{P}), \tag{3.4}$$

where the $ad_{{}^BT_B^I}$ is the adjoint of the body twist, which represents the fictitious forces that arise on using a non-inertial frame, is defined as follows:

$$ad_{{}^BT_B^I} = \begin{pmatrix} {}^B\tilde{\omega}_B^I & \boldsymbol{0_{3\times 3}} \\ {}^B\tilde{v}_B^I & {}^B\tilde{\omega}_B^I \end{pmatrix} \in \mathbb{R}^{6\times 6}. \tag{3.5}$$

Introducing the skew-symmetric matrix $\boldsymbol{J(P)} = -\boldsymbol{J(P)}^{\top} \in \mathbb{R}^{6\times 6}$, such that:

$$\boldsymbol{J(P)} = \begin{pmatrix} \tilde{\boldsymbol{P}}_{\boldsymbol{\omega}} & \tilde{\boldsymbol{P}}_{\boldsymbol{v}} \\ \tilde{\boldsymbol{P}}_{\boldsymbol{v}} & \boldsymbol{0}_{3\times 3} \end{pmatrix}, \qquad \boldsymbol{P} = \begin{pmatrix} \boldsymbol{P}_{\boldsymbol{\omega}} \\ \boldsymbol{P}_{\boldsymbol{v}} \end{pmatrix}, \tag{3.6}$$

$\tilde{\boldsymbol{P}}_{\boldsymbol{\omega}}, \tilde{\boldsymbol{P}}_{\boldsymbol{v}} \in so^*(3)$ are the skew-symmetric matrices of $\boldsymbol{P}_{\boldsymbol{\omega}}, \boldsymbol{P}_{\boldsymbol{v}} \in (\mathbb{R}^3)^*$. They are also co-vectors of the angular and linear components of the twist, respectively. When paired together, they correspond to twice of the kinetic energy of the body, i.e, $\langle \boldsymbol{P}|\boldsymbol{T}\rangle = \boldsymbol{P}^{\top}\boldsymbol{T} = \boldsymbol{P}_{\boldsymbol{\omega}}^{\top}\boldsymbol{\omega} + \boldsymbol{P}_{\boldsymbol{v}}^{\top}\boldsymbol{v} = \boldsymbol{\omega}^{\top}\boldsymbol{J}^{\top}\boldsymbol{\omega} + \boldsymbol{m}\boldsymbol{v}^{\top}\boldsymbol{v}$

Equation 3.4 can be reformulated as a matrix multiplication of the effort variable as follows:

$$\dot{\boldsymbol{P}} = \boldsymbol{J(P)T} = \boldsymbol{J(P)}\partial_{\boldsymbol{P}}\boldsymbol{\mathcal{H}}_k. \tag{3.7}$$

Since the system so far has no extenal ports, the Hamiltonian (kinetic energy of the system) is conserved and this can be proven by checking the rate of change of the Hamiltonian.

$$\dot{\boldsymbol{\mathcal{H}}}_k = \langle \partial_P \boldsymbol{\mathcal{H}}_k | \dot{\boldsymbol{P}} \rangle_{(\mathbb{R}^6)^*} = \partial_P^{\top}\boldsymbol{\mathcal{H}}_k J(P)\partial_P\boldsymbol{\mathcal{H}}_k = 0. \tag{3.8}$$

Thanks to the skew-symmetric property of the Dirac structure present in $\boldsymbol{J(P)}$, conservation of kinetic energy is implied.

In Bond graph notation, equation 3.7 is represented as shown in figure 3.2a. For the consistency of the modeling approach, Dirac structures of rigid bodies will have their power ports all inwards. Thus, equation 3.7 is rewritten as follows:

$$-\dot{\boldsymbol{P}} = -\boldsymbol{J(P)}\partial_{\boldsymbol{P}}\boldsymbol{\mathcal{H}} = \boldsymbol{J}^{\top}\boldsymbol{(P)}\partial_{\boldsymbol{P}}\boldsymbol{\mathcal{H}}. \tag{3.9}$$

In bond graph notation, a **0-** junction is added to reverse power direction as shown in figure 3.2b.

(a) Bond graph representation of equation 3.7

(b) Bond graph representation of equation 3.9 with power ports **into** the Dirac Structure

Figure 3.2: Closed model of the kinetic energy of a rigid body.

Interaction port

An extra interaction port is added to model external forces applied on the rigid body. Equations 3.4 and 3.9 are then modified to include the external wrench applied.

$$-\dot{\boldsymbol{P}} = \boldsymbol{J}^\top(\boldsymbol{P})\boldsymbol{\partial_P \mathcal{H}} - {}^{\boldsymbol{B}}\boldsymbol{W_{ext}}, \tag{3.10}$$

where ${}^{\boldsymbol{B}}\boldsymbol{W_{ext}} \in \mathbb{R}^6$ is the external wrench applied on the rigid body expressed in the body-fixed frame.

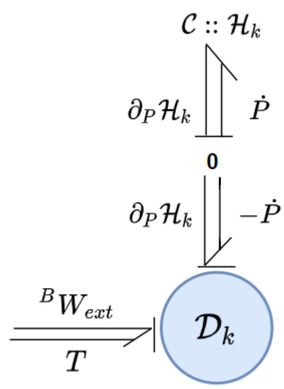

Figure 3.3: Open model of the kinetic energy of the rigid body including an interaction port

The Dirac structure $\boldsymbol{\mathcal{D}}_k$ shown above is then defined as follows:

$$\begin{pmatrix} -\dot{\boldsymbol{P}} \\ \boldsymbol{T} \end{pmatrix} = \begin{pmatrix} \boldsymbol{J}^\top(\boldsymbol{P}) & -\boldsymbol{I}_{6\times 6} \\ \boldsymbol{I}_{6\times 6} & \boldsymbol{0}_{6\times 6} \end{pmatrix} \begin{pmatrix} \boldsymbol{\partial_P \mathcal{H}}_k \\ {}^{\boldsymbol{B}}\boldsymbol{W_{ext}} \end{pmatrix}. \tag{3.11}$$

The skew-symmetric property of Dirac structures is confirmed here. Now, the system has an external port which means that the energy balance has an external power supply coming from the external wrench. To confirm that:

$$\dot{\boldsymbol{\mathcal{H}}}_k = \langle \dot{\boldsymbol{P}} | \partial_P \boldsymbol{\mathcal{H}}_k \rangle_{(\mathbb{R}^6)^*} = \partial_P^\top \boldsymbol{\mathcal{H}}_k J^\top(P) \partial_P \boldsymbol{\mathcal{H}} + W^\top \partial_P \boldsymbol{\mathcal{H}} = 0 + W^\top T, \tag{3.12}$$

which is the power supplied by the external wrench. Figure 3.3 shows the bond graph representation of the open model of the kinetic energy.

Potential Energy

The potential energy of a body in space due to gravity is defined by the Hamiltonian $\mathcal{H}_g$:

$$\mathcal{H}_g(\boldsymbol{H}) = m\boldsymbol{\xi}^\top g, \tag{3.13}$$

where m is the mass of the body, $g \in \mathbb{R}^3$ is the inverse direction of the gravitational acceleration in the inertial frame. $\boldsymbol{\xi} \in \mathbb{R}^3$ is the translation component of the body's configuration. The full configuration of the body $\boldsymbol{H} \in SE(3)$ is defined as follows:

$$\boldsymbol{H} = \begin{pmatrix} \boldsymbol{R} & \boldsymbol{\xi} \\ \boldsymbol{0}_{1\times 3} & \boldsymbol{1} \end{pmatrix}, \qquad \boldsymbol{R} \in SO(3), \tag{3.14}$$

where $\boldsymbol{R}$ is the Rotation matrix of the body with respect to the inertial frame.

Checking the energy balance of the Hamiltonian:

$$\dot{\mathcal{H}}_{\boldsymbol{g}} = \langle \partial_H \mathcal{H} | \dot{H} \rangle_{SE(3)} = \langle \partial_R \mathcal{H} | \dot{R} \rangle_{SO(3)} + \langle \partial_\xi \mathcal{H} | \dot{\xi} \rangle_{\mathbb{R}^3} = 0 + \langle \partial_\xi \mathcal{H} | \dot{\xi} \rangle_{\mathbb{R}^3} = mg^\top \dot{\xi}. \tag{3.15}$$

This implies that there is power being supplied to the system through the gravitational force.

The *flow* is the rate of change of the state variable $\boldsymbol{H}$, defined as $\dot{\boldsymbol{H}} \in T_H SE(3)$ where, $T_H SE(3)$ is the tangent space of the Special Euclidean group at the specific configuration $\boldsymbol{H}$.

$$\dot{\boldsymbol{H}} = \boldsymbol{H}\tilde{\boldsymbol{T}} = \boldsymbol{\chi}_{\boldsymbol{H}}(\boldsymbol{T}). \tag{3.16}$$

where $\chi_H : \mathbb{R}^6 \longrightarrow T_H SE(3)$ is the map from $\mathbb{R}^6$ to the tangent space of the Special Euclidean group at the configuration $\boldsymbol{H}$, defined as follows:

$$\chi_H := (L_H)_{*,I} \circ \tilde{S}. \tag{3.17}$$

The map $\tilde{S} : \mathbb{R}^6 \longrightarrow se(3)$ is the tilde operation applied on the twist and $(L_H)_{*,I}$ is the pushforward left transnational map $(L_H)_{*,I} : se(3) \longrightarrow T_H SE(3)$. Since $SE(3)$ is a matrix Lie group, the pushforward map can be expressed using matrix multiplication.

The *effort* is the change of the Hamiltonian $\mathcal{H}_g$ with respect to the state variable $\boldsymbol{H}$, which corresponds to the gravitational force affecting the body expressed in body-fixed frame $W_g \in (\mathbb{R}^6)^*$.

Due to the skew-symmetric property of the Dirac structure, the relation between $\partial_H \mathcal{H}_g$ and W_g can be easily driven by the dual map $\boldsymbol{\chi}_H^* : T_H^* SE(3) \longrightarrow (\mathbb{R}^6)^*$.

The dual map is defined as:

$$\boldsymbol{\chi}_H^* := \tilde{S}^* \circ (L_H)_I^*. \tag{3.18}$$

$$(L_H)_I^* : T_H^* SE(3) \longrightarrow se^*(3), \qquad \tilde{S}^* : se^*(3) \longrightarrow (\mathbb{R}^6)^*. \tag{3.19}$$

$\boldsymbol{(L_H)_I^*}$ is the push-backwards left transnational map and $\boldsymbol{\tilde{S}^*}$ is the dual map of $\boldsymbol{\tilde{S}}$, corresponds to the inverse of the tilde operation. Thus system equation can be finalised as:

$$\begin{pmatrix} \dot{\boldsymbol{H}} \\ \boldsymbol{W_g} \end{pmatrix} = \begin{pmatrix} \boldsymbol{0} & \boldsymbol{\chi_H} \\ -\boldsymbol{\chi}_{\boldsymbol{H}}^{\boldsymbol{*}} & \boldsymbol{0} \end{pmatrix} \begin{pmatrix} \partial_H \mathcal{H}_g \\ \boldsymbol{T} \end{pmatrix}. \tag{3.20}$$

Figure 3.4 shows the bond graph of the Dirac structure representing the potential energy of the rigid body.

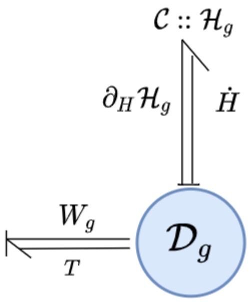

Figure 3.4: Potential energy model of a rigid body

Final Rigid Body Model

Adding both the open model of the kinetic energy with the potential energy, the Dirac structure $\mathcal{D}_t$ is then defined:

$$\begin{pmatrix} -\dot{\boldsymbol{H}} \\ -\dot{\boldsymbol{P}} \\ \boldsymbol{T} \end{pmatrix} = \begin{pmatrix} \boldsymbol{0} & -\boldsymbol{\chi}_H & \boldsymbol{0} \\ \boldsymbol{\chi}_H^* & -\boldsymbol{J}(\boldsymbol{P}) & -\boldsymbol{I} \\ \boldsymbol{0} & \boldsymbol{I} & \boldsymbol{0} \end{pmatrix} \begin{pmatrix} \boldsymbol{\partial_H \mathcal{H}_g} \\ \boldsymbol{\partial_P \mathcal{H}_k} \\ {}^B\boldsymbol{W_{ext}} \end{pmatrix}. \tag{3.21}$$

Connecting both storage elements for the kinetic and potential energies, the total Hamiltonian is then $\mathcal{H}_t = \mathcal{H}_k + \mathcal{H}_g = \frac{1}{2}\boldsymbol{P}^\top \boldsymbol{\mathcal{I}}^{-1}\boldsymbol{P} + m\boldsymbol{\xi}^\top g$.
Last step is introducing the state variable $\boldsymbol{x} := (\boldsymbol{H}, \boldsymbol{P}) \in SE(3) \times (\mathbb{R}^6)^*$.
The *flow* and *effort* variables are then defined as:

$$\dot{\boldsymbol{x}} = \begin{pmatrix} \dot{\boldsymbol{H}} \\ \dot{\boldsymbol{P}} \end{pmatrix}, \qquad \boldsymbol{\partial_x \mathcal{H}_t} = \begin{pmatrix} \boldsymbol{\partial_H \mathcal{H}_g} \\ \boldsymbol{\partial_P \mathcal{H}_k} \end{pmatrix}. \tag{3.22}$$

Equation 3.21 can be written as:

$$\begin{pmatrix} -\dot{\boldsymbol{x}} \\ \boldsymbol{T} \end{pmatrix} = \begin{pmatrix} -\boldsymbol{J_{RB}} & -\boldsymbol{G} \\ \boldsymbol{G}^\top & \boldsymbol{0} \end{pmatrix} \begin{pmatrix} \boldsymbol{\partial_x \mathcal{H}_t} \\ {}^B\boldsymbol{W_{ext}} \end{pmatrix}, \tag{3.23}$$

where,

$$\boldsymbol{J_{RB}} = \begin{pmatrix} \boldsymbol{0} & \boldsymbol{\chi_H} \\ -\boldsymbol{\chi}_H^* & \boldsymbol{J}(\boldsymbol{P}) \end{pmatrix}, \qquad \boldsymbol{G} = \begin{pmatrix} \boldsymbol{0} \\ \boldsymbol{I} \end{pmatrix}, \qquad \boldsymbol{G}^\top = \begin{pmatrix} \boldsymbol{0} & \boldsymbol{I} \end{pmatrix}.$$

In *input-state-output* formulation, equation 3.21 is written as:

$$\begin{pmatrix} \dot{\boldsymbol{H}} \\ \dot{\boldsymbol{P}} \end{pmatrix} = \begin{pmatrix} \boldsymbol{0} & \boldsymbol{\chi_H} \\ -\boldsymbol{\chi}_H^* & \boldsymbol{J}(\boldsymbol{P}) \end{pmatrix} \begin{pmatrix} \boldsymbol{\partial_H \mathcal{H}_g} \\ \boldsymbol{\partial_P \mathcal{H}_k} \end{pmatrix} + \begin{pmatrix} \boldsymbol{0} \\ \boldsymbol{I} \end{pmatrix} \boldsymbol{W_{ext}}, \tag{3.24}$$

$$\boldsymbol{T} = \begin{pmatrix} \boldsymbol{0} & \boldsymbol{I} \end{pmatrix} \begin{pmatrix} \boldsymbol{\partial_H \mathcal{H}_g} \\ \boldsymbol{\partial_P \mathcal{H}_k} \end{pmatrix}, \tag{3.25}$$

which is equivalent to:

$$\dot{\boldsymbol{x}} = \boldsymbol{J_{RB}} \boldsymbol{\partial_x \mathcal{H}_t} + \boldsymbol{G}^B \boldsymbol{W_{ext}}, \tag{3.26}$$

$$\boldsymbol{T} = \boldsymbol{G}^\top \boldsymbol{\partial_x \mathcal{H}_t}. \tag{3.27}$$

The bond graph representation of the full model of the rigid body is shown in figure 3.5.

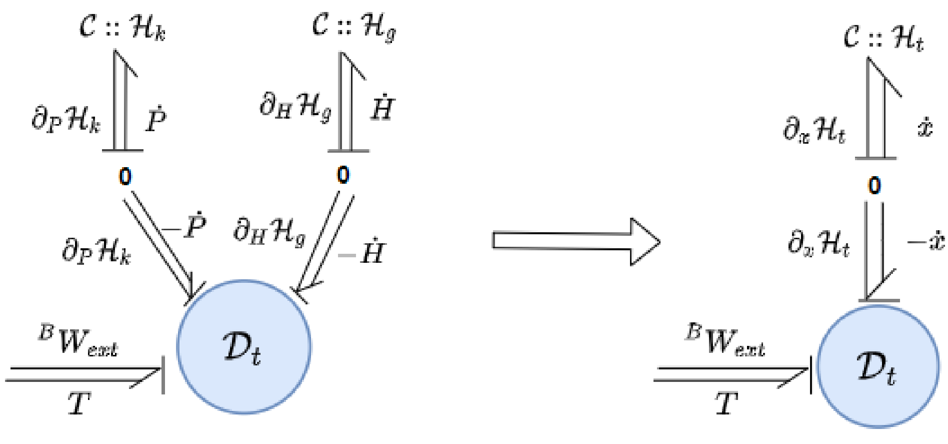

Figure 3.5: Final port Hamiltonian model in the bond graph notation

3.1.2 Analogy to Bond Graph

One analogous way of looking at rigid body modeling is to use Netwon's 2nd law in the bond graph notation. This gives a bond graph model which is analogous to the open Port Hamiltonian model shown above. The systematic procedure works as follows:

- To apply Newton's 2^{nd} law, a **1-** junction is used for the summation of the forces.
- **I-** type storage element is used to model the storage of kinetic energy in the system, it contains information about the inertia tensor ${}^B\mathcal{I}$.
- **MGY** a modulated gyrator is used to model the fictitious forces $\boldsymbol{J}(\boldsymbol{P})$.
- Gravitational Force is modeled as an external source of effort **Se**.
- A modulated transformer **MTF** is used to tranform wrench from the gravity-fixed frame to the body-fixed frame. The gravitational frame is a frame with its origin attached to the body-fixed frame,and its z-axis parallel to the that of the world frame.
- Finally, a **Se** is used to model external wrenches applied on the body expressed in the body-fixed frame ${}^B W_{ext}$.

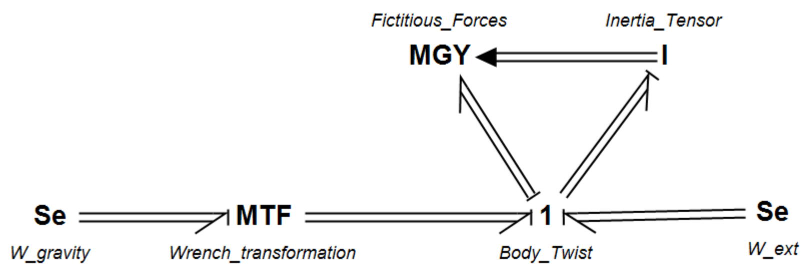

Figure 3.6: Bond graph representation of a rigid body in space

In this section, derivation of rigid body modeling in the Port Hamiltonian framework was studied. Moreover, the analogous representation in the bond graph notation was also discussed. It is to be noted that the rigid body modeling in the bond graph notation had a preferred **integral** causality. In the next sections, the same steps will be used for modeling the multi-body dynamics of a flapping-wing UAV.

3.2 Kinematics of the Robird

The Robird, in its simplest form, consists of three rigid bodies (one base body and two wings) connected to each other by two active revolute joints.

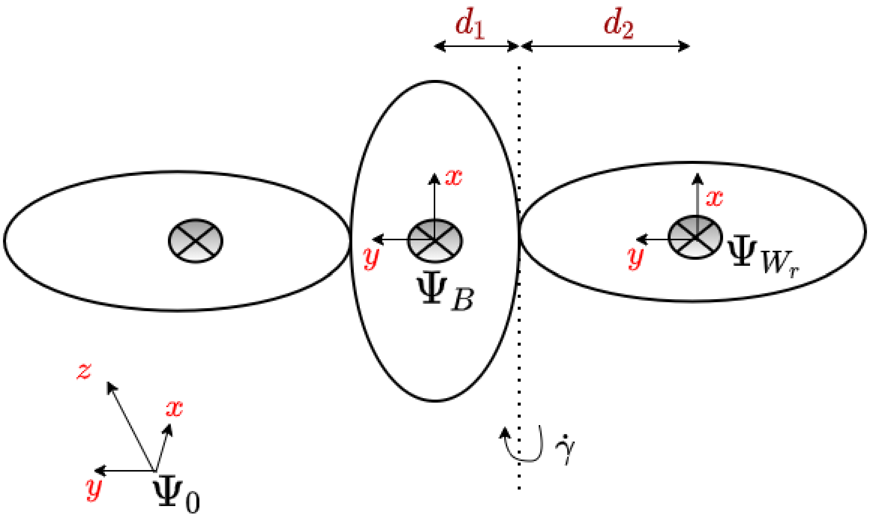

Figure 3.7: Simplified kinematic model of the Robird

3.2.1 Frames

For each rigid body, there is a body-fixed frame, with its origin at the center of mass of the body. $x-axis$ points forward, $y-axis$ points to the left and $z-axis$ is directed upwards. Its assumed that all center of masses lie on the the same $y-$ level. As shown in figure 3.7, Ψ_B represents the body-fixed frame of the base body.

Due to the symmetry of the Robird, kinematics will be studied on only the right wing and same theory applies on the left one. For the rest of the chapter Ψ_W denotes the body-fixed frame of the right wing. Ψ_0 is the ground (inertial) frame.

3.2.2 Flapping Mechanism

Flapping occurs by rotation around the dotted line in the above figure. This axis is parallel to the $x-axis$ of the base body-fixed frame. A one dimensional rotational joint is used to flap the wing back and forth. It can be seen that the wing is a rigid body connected to a moving base which is the base body of the Robird. Thanks to the geometric representation of the system, **unit twists** can be used to model this actuation, such that the twist of the wing relative to the base body expressed in the base body frame is defined as:

$$^{B}\boldsymbol{T}_{W}^{B} = {}^{B}\hat{\boldsymbol{T}}_{W}^{B} \cdot \dot{\boldsymbol{\gamma}}, \tag{3.28}$$

where $\dot{\gamma}$ is the angular velocity imposed by the actuator. ${}^{B}\hat{\boldsymbol{T}}_{W}^{B}$ is the unit twist defined as follows:

$$^{B}\hat{\boldsymbol{T}}_{W}^{B} = \begin{pmatrix} \hat{\boldsymbol{\omega}} \\ r \wedge \hat{\boldsymbol{\omega}} \end{pmatrix}, \tag{3.29}$$

where r is the distance between the axis of rotation and the frame it is expressed in. For the right wing, $r_y = -d_1$.

$$
{}^B\hat{T}_W^B = \begin{pmatrix} \mathbf{1} \\ \mathbf{0} \\ \mathbf{0} \\ \begin{pmatrix} \mathbf{0} \\ -\boldsymbol{d_1} \\ \mathbf{0} \end{pmatrix} \wedge \begin{pmatrix} \mathbf{1} \\ \mathbf{0} \\ \mathbf{0} \end{pmatrix} \end{pmatrix} = \begin{pmatrix} \mathbf{1} \\ \mathbf{0} \\ \mathbf{0} \\ \mathbf{0} \\ \mathbf{0} \\ \boldsymbol{d_1} \end{pmatrix}. \tag{3.30}
$$

3.3 Dynamic Model of the Robird

Thanks to the port-based modeling approach used in this thesis, the Robird can be divided easily into a set of sub-systems connected to each other by power ports, then each sub-system will be treated separately. As said earlier, the Robird has two flapping wings and two movable tails. Since in this work, the focus is on the aerodynamic contribution resulting from wings' flapping, the tails will be ignored in this preliminary dynamic model. However, they can be easily included as sub-systems through power ports to the base body. The Robird will then be treated as three rigid bodies, base body representing the hull and two flapping wings. Each wing is connected to the base body through an actuator.

Figure 3.8: Top view of the Robird

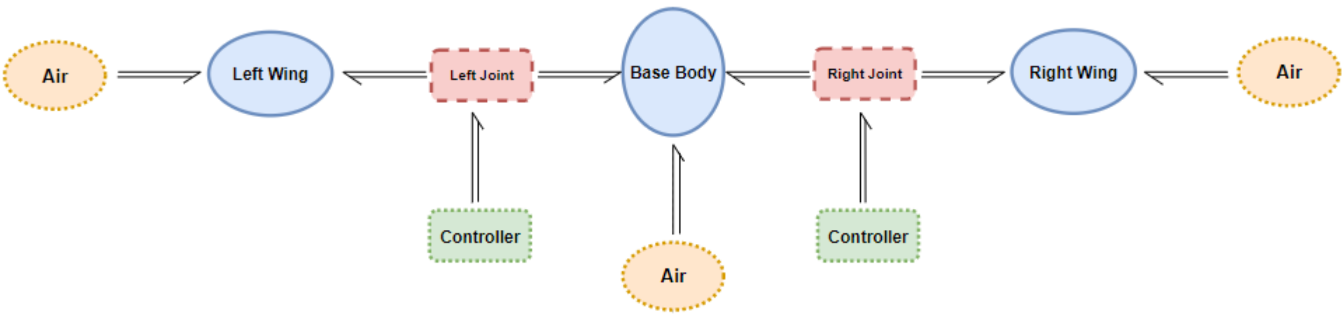

Figure 3.9: Simplified Port-based representation of the Robird

Due to the symmetry of the Robird, one half will be studied and results apply on the other half. This section is divided into three sub-sections for each sub-system: the base body, the joint and the wing. For each sub-section, the port-Hamiltonian dynamic model and the bond graph implementation are shown. The trick is to define the **Dirac Structure** of each sub-system.

3.3.1 Base Body Modeling

The base body is a rigid body with two external ports that represent coming wrenches from both wings, ${}^{B}W_{lw}, {}^{B}W_{rw}$, representing the wrench coming from the left and right wing, respectively. These wrenches do not only contain information about the aerodynamic forces affecting the wing, but also inertial forces on the wing including gravitational forces. Both wrenches are expressed in the base-body-fixed frame. Thanks to the port-based formulation, ports can be easily added and the Dirac structure will be updated.
Figure 3.10 shows the bond graph representation of the base body in two different equivalent formats as discussed earlier. In the first representation, potential and kinetic energies are treated as separate storage variables, with state variables P, H, respectively. Whereas in the latter representation, they are combined into one storage variable with a state variable x.

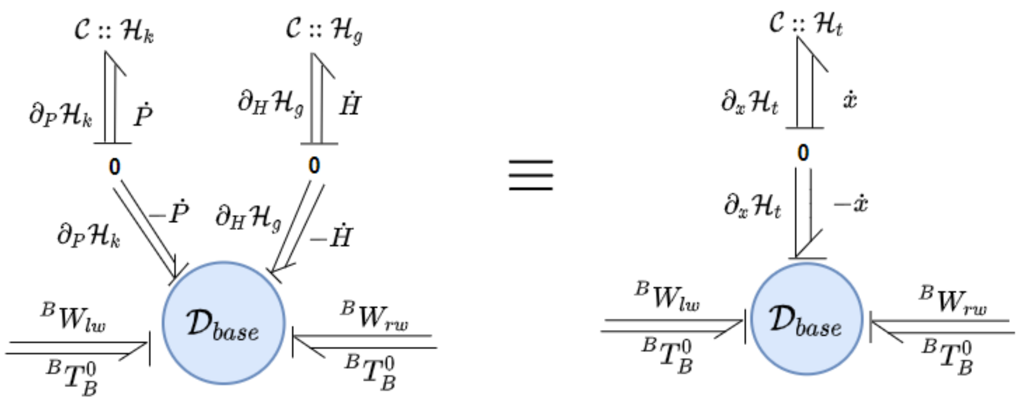

Figure 3.10: Bond graph representation of the Base Body in the Port Hamiltonian Framework

The Dirac structures are then defined as follows:

$$\begin{pmatrix} -\dot{H} \\ -\dot{P} \\ {}^{B}T_B^0 \\ {}^{B}T_B^0 \end{pmatrix} = \begin{pmatrix} 0 & -\chi_H & 0 & 0 \\ \chi_H^* & -J(P) & -I & -I \\ 0 & I & 0 & 0 \\ 0 & I & 0 & 0 \end{pmatrix} \begin{pmatrix} \partial_H \mathcal{H}_g \\ \partial_P \mathcal{H}_k \\ {}^{B}W_{lw} \\ {}^{B}W_{rw} \end{pmatrix}, \qquad \begin{pmatrix} -\dot{x} \\ {}^{B}T_B^0 \\ {}^{B}T_B^0 \end{pmatrix} = \begin{pmatrix} -J_{RB} & -G & -G \\ G^\top & 0 & 0 \\ G^\top & 0 & 0 \end{pmatrix} \begin{pmatrix} \partial_x \mathcal{H}_t \\ {}^{B}W_{lw} \\ {}^{B}W_{rw} \end{pmatrix} \tag{3.31}$$

3.3.2 Wing Modeling

The right wing will be modeled in this sub-section and same theory applies on the left wing. The wing is modeled as a rigid body with two interaction ports as well. The first one is due aerodynamic contribution acting **on** the wing represented in ${}^{W}W_{air}$, expressed in the wing frame. The second one is the wrench caused **by** the wing and affecting the base body. This wrench is represented by $-{}^{W}W_{rw}$. The negative sign indicates that the wrench is caused **by** the wing. One last thing, since we are interested in the wrench caused by the wing on the base body, it is seen as the output of the dynamic equation. This implies a change in the causality of the open kinetic energy model, as shown in figure 3.11.
Thus, the Dirac structure of the wing sub-system is represented as:

$$\begin{pmatrix} -\dot{H} \\ \partial_P \mathcal{H}_k \\ {}^{W}T_W^0 \\ -{}^{W}W_{rw} \end{pmatrix} = \begin{pmatrix} 0 & 0 & 0 & -\chi_H \\ 0 & 0 & 0 & I \\ 0 & 0 & 0 & I \\ \chi_H^* & -I & -I & -J(P) \end{pmatrix} \begin{pmatrix} \partial_H \mathcal{H}_g \\ -\dot{P} \\ {}^{W}W_{air} \\ {}^{W}T_W^0 \end{pmatrix} \tag{3.32}$$

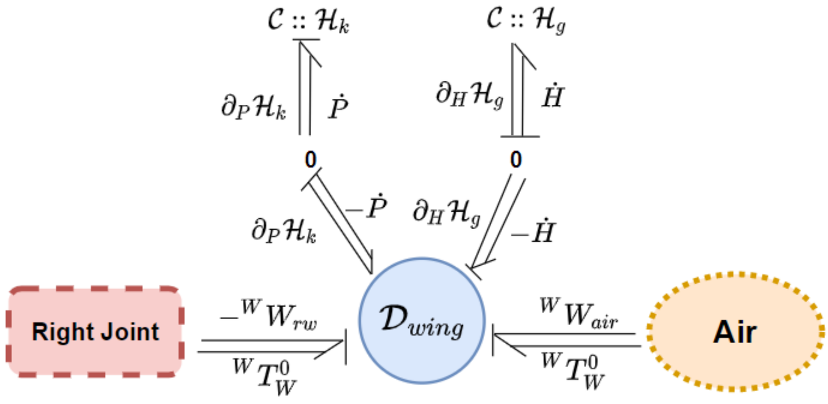

Figure 3.11: Bond graph representation of the wing in the Port-Hamiltonian framework

3.3.3 Joint Modeling

From the kinematics, the twist of the base body ${}^B\boldsymbol{T}_{\boldsymbol{B}}^{\boldsymbol{0}}$ and that of the wing ${}^W\boldsymbol{T}_{\boldsymbol{W}}^{\boldsymbol{0}}$ along with the control input $\dot{\boldsymbol{\gamma}}$ can be related as follows:

$$\begin{aligned} {}^W T_W^0 &= Ad_{{}^W H_B}({}^B T_W^0) = Ad_{{}^W H_B}({}^B T_B^0 + {}^B T_W^B) \\ &= Ad_{{}^W H_B}({}^B T_B^0 + {}^B \hat{T}_W^B \cdot \dot{\gamma}) \end{aligned} \tag{3.33}$$

Similarly, using wrench transformation:

$$\begin{aligned} {}^B W_{rw} &= Ad^\top_{{}^W H_B}({}^W W_{rw}) \\ &= -Ad^\top_{{}^W H_B}(-{}^W W_{rw}) \end{aligned} \tag{3.34}$$

For the derivation of torque of the actuator $\boldsymbol{\tau}$, power equations are used. Since the actuator is assumed to be an ideal without losses, power at the joint equals to the power delivered to flap the wings. The full derivation of the torque equation is given below.

$$\begin{aligned} \tau^\top \dot{\gamma} &= {}^B W_{rw}^\top \, {}^B T_W^B \\ \tau^\top \dot{\gamma} &= {}^B W_{rw}^\top \, {}^B \hat{T}_W^B \cdot \dot{\gamma} \\ \tau^\top &= {}^B W_{rw}^\top \, {}^B \hat{T}_W^B \\ \tau^\top &= (-Ad^\top_{{}^W H_B}(-{}^W W_{rw}))^\top \, {}^B \hat{T}_W^B \\ \tau^\top &= -(-{}^W W_{rw})^\top Ad_{{}^W H_B} \hat{T}_W^B \end{aligned}$$

Thus,

$$\tau = -(\hat{T}_W^B)^\top Ad^\top_{{}^W H_B}(-{}^W W_{rw}) \tag{3.35}$$

The bond graph representation of the joint sub-system is shown in figure 3.12
In a skew-symmetric matrix representation, the final Dirac structure of the joint is expressed as:

$$\begin{pmatrix} {}^W\boldsymbol{T}_{\boldsymbol{W}}^{\boldsymbol{0}} \\ {}^B\boldsymbol{W}_{\boldsymbol{rw}} \\ \boldsymbol{\tau} \end{pmatrix} = \begin{pmatrix} \boldsymbol{0} & \boldsymbol{Ad}_{{}^W\boldsymbol{H_B}} & \boldsymbol{Ad}^{\boldsymbol{B}}_{{}^W\boldsymbol{H_B}} \hat{\boldsymbol{T}}_{\boldsymbol{W}}^{\boldsymbol{B}} \\ -\boldsymbol{Ad}^\top_{{}^W\boldsymbol{H_B}} & \boldsymbol{0} & \boldsymbol{0} \\ -(\hat{\boldsymbol{T}}_{\boldsymbol{W}}^{\boldsymbol{B}})^\top \boldsymbol{Ad}^\top_{{}^W\boldsymbol{H_B}} & \boldsymbol{0} & \boldsymbol{0} \end{pmatrix} \begin{pmatrix} -{}^W\boldsymbol{W}_{\boldsymbol{rw}} \\ {}^B\boldsymbol{T}_{\boldsymbol{B}}^{\boldsymbol{0}} \\ \dot{\boldsymbol{\gamma}} \end{pmatrix} \tag{3.36}$$

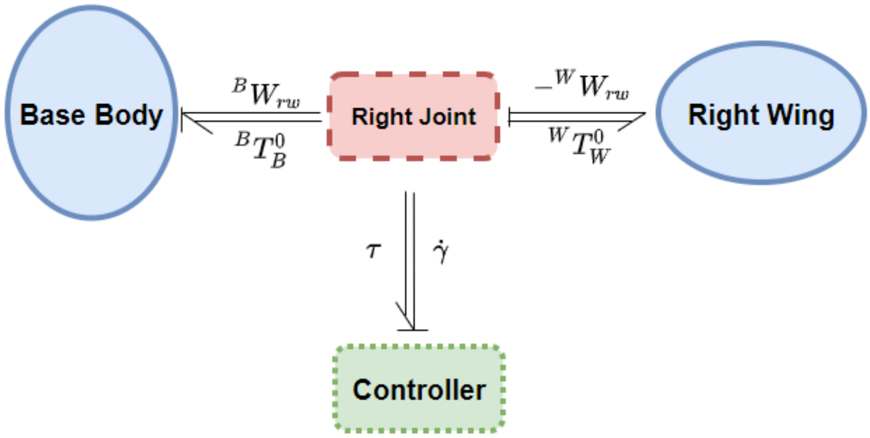

Figure 3.12: Bond graph representation of the joint in the Port Hamiltonian Framework

3.4 Conclusion

This chapter started with a systematic procedure to model rigid body motion in the Port-Hamiltonian framework. In this framework, the system was viewed as an interconnection of sub-systems of storage elements and an external port. This procedure focuses on driving the Dirac structure of the network in a skew-symmetric matrix representation. The Port Hamiltonian model is an open model which allows for interaction with other sub-systems. This can include interaction with the environment (such as the air) or the controller. Thus, this eases the way of rigid body modeling for future control purposes.

The systematic way was also applied on a multi-body flapping-wing UAV, where the Robird was taken as a study case. First, kinematics of a preliminary model of the Robird was presented. Then, multi-body modeling was performed using the port-Hamiltonian framework presented. Thanks to the port-based thinking exhibited in this thesis, it is easy to connect different ports to the preliminary model. The aerodynamic effects are seen as an external port connected to each of the wings. However, in this chapter, the aerodynamic constitutive relations are still unknown. The goal of the next chapter is to derive these constitutive relations and give an expression for the aerodynamic forces affecting each wing. Thus, the dynamic model presented becomes a full model that includes aerodynamics of flapping flight.

4 Aerodynamic Model

This chapter explains the aerodynamic constitutive relations, expressed in the connection between the air and each wing . The adopted aerodynamic model in this thesis is the one developed by *DeLaurier* in 1993 (8). The model was chosen for several reasons: First of all, flapping flight is unsteady and using quasi-steady aerodynamic models do not hold. In literature, quasi-steady models have been used for control purposes, due to its simplifications form. However, these models have many assumptions and are not strong enough to capture the unsteady phenomena due to flapping. For example, quasi-steady models work for low flapping frequency thus wake effects are ignored. On the other hand, Delaurier's model is a design-oriented model that accounts for unsteady aerodynamics. The model takes into account the following unsteady phenomena:

- Vortex-wake effects
- Camber Partial edge suction
- Post stall behaviour
- Apparent mass effect
- Viscous flow around the wing
- Down-wash effect

With that being said, this model is stronger than quasi-steady models used in literature. Furthermore, this model takes into account flexibility of the wing, including twist and bending. Last but not least, the model assumes the following assumptions:

- Flapping is achieved by a continuous sinusoidal motion.
- Upstroke and downstroke have equal times intervals.
- Aspect ratio of the wing should be high so that the flow around each section is essentially chordwise.

Finally, the model uses a modified strip theory approach where the wing is divided into strips along its span, as shown in figure 4.1. Each strip is then treated individually as an airfoil assumed to be part of an elliptical planform wing equivalent to the real wing (same aspect ratio and performing same harmonic motion).
This chapter can be seen as an explanation of Delaurier's model (8) following the same port-based apporach used in this thesis. Kinematics of wing flapping is explained first and related to geometric screw theory mentioned before. Finally, dynamics of the aerodynamic model are shown.

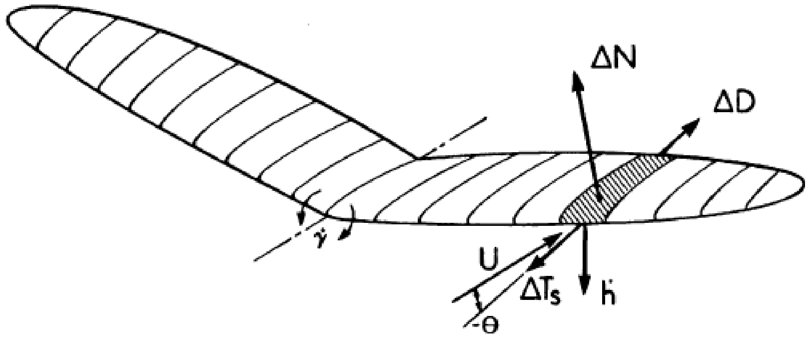

Figure 4.1: Strip theory applied on a wing (8)

4.1 Kinematics

4.1.1 Flapping Profile

The wing flaps back and forth in y-z plane, in a sinusoidal harmonic motion, such that the flapping angle is defined, as shown in figure 4.2, as:

$$\gamma(t) = \Gamma sin(\omega t), \tag{4.1}$$

where Γ is the maximum flapping angle and ω is the flapping frequency. Due to flapping, there is a plunging motion expressed as:

$$h(t) = y\gamma(t) = \Gamma y sin(\omega t), \tag{4.2}$$

such that y varies with the span wise airfoil section being studied. For example, at the root $y = 0$, and at the wing tip $y = b/2$, where b is the span length. h is chosen to be positive downwards.

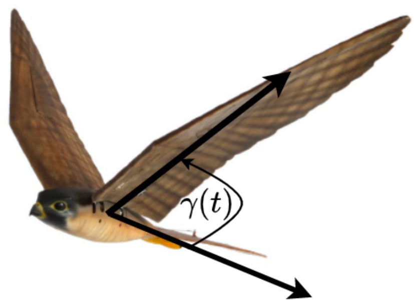

Figure 4.2: Flapping angle γ of the Robird

4.1.2 Angle Calculations

There are several angles that play an important rule in the output wrench on the wing. Figure 4.3 shows the relevant angles for an airfoil section. These angles are:

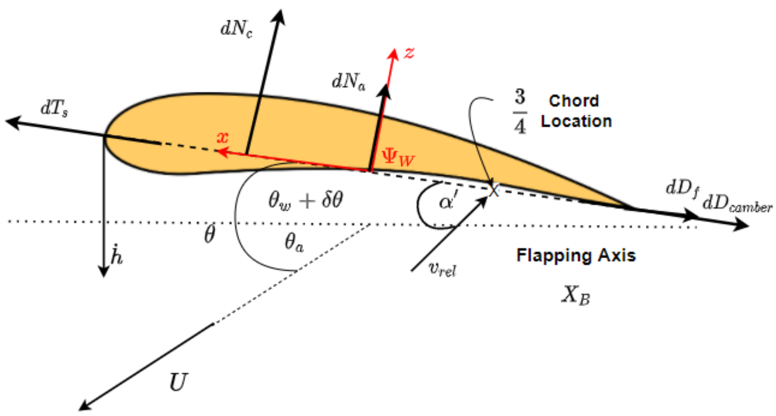

Figure 4.3: Airfoil section including motion variables and generated forces

Body's pitch angle ($\boldsymbol{\theta_a}$)

θ_a is the pitch angle of the base body. In other words, its the angle between the flapping axis and the direction of flight. $\boldsymbol{\theta_a}$ can be related to the twist of the base body $^{\boldsymbol{B}}\boldsymbol{T_B^0}$ as follows:

$$\theta_a = tan^{-1}(\frac{(v_B)_z}{(v_B)_x}), \qquad {}^B T_B^0 = \begin{pmatrix} \omega_B \\ v_B \end{pmatrix}, \qquad and \qquad U = ||v_B||. \tag{4.3}$$

Wing's pitch angle ($\boldsymbol{\theta_w}$)

The model adopted in this dissertation accounts for pitching of the wing. θ_w is the pitch angle of the wing relative to the $x-axis$ of the base body-fixed frame. In case of active pitching, θ_w is a function of time. For the Robird, the wing's pitch angle is assumed to vary with the same frequency as flapping but with a phase shift (11).

$$\theta_w(t) = \theta_{w0} sin(\omega t + \phi), \tag{4.4}$$

where ϕ is the phase shift between plunging and pitching motion. θ_{w0} is the maximum pitch angle. In case of passive pitching, θ_w is constant.

Pitch angle Deflection along the wing ($\delta\theta$)

One of the strong points of the model used in this work, is that it accounts for flexible wings. $\delta\theta$ is the deflection angle along the wing. In this dissertation, the wing is treated as a rigid body so $\delta\theta = 0$.

Total Pitch angle ($\boldsymbol{\theta}$)

The total pitch angle of each airfoil section is the summation of the previous mentioned angles,

$$\theta = \theta_a + \theta_w. \tag{4.5}$$

Relative angle of attack ($\boldsymbol{\alpha}$)

α is the relative angle of attack at the $\frac{3}{4}$ chord-location due to wing's motion. It can be seen as the geometric angle of attack of the system. The wing's motion can be decomposed into three main discrete motions: plunging, pitching and forward motion relative to the free stream velocity. The relative angle of attack accounts for these motions as follows:

$$\alpha = \frac{\dot{h} cos(\theta_w) + \frac{3}{4} c\dot{\theta} + U \cdot \delta\theta}{U} \tag{4.6}$$

The first term is the component of the plunging velocity $\dot{\boldsymbol{h}}$ normal to the airfoil chord, expressed as $\dot{h}cos(\theta_w)$. The second component is due to pitching of the wing around the $\frac{3}{4}$ chord location. Thus, the radius is $\frac{3}{4}c$ and the rotational velocity is $\frac{3}{4}c \cdot \dot{\theta}$. The final motion accounted for is the due to the deflection of the wing in the forward motion $U \cdot \delta\theta$. In our case, this term equals to zero since the wing is a rigid body.

Flow's relative angle of attack $\boldsymbol{\alpha'}$

Finally, due to the unsteadiness of the flow, the effective angle of attack after at the $\frac{3}{4}$ chord location should be modified. $\boldsymbol{\alpha'}$ takes into account **unsteady wake** and **downwash effects**.

$$\alpha' = C'_{Jones}(k)\alpha - \frac{w_0}{U}. \tag{4.7}$$

The unsteady wake is modeled by Modified *Theodorsen Function (18)* expressed in the term $C'_{Jones}(k)$. For a more convenient formulation, according to *Scherer (30)*:

$$C'_{Jones}(k) = \left[\frac{AR \cdot C'(k)}{2+AR}\right],$$

defined as the complex function $C'(k) = F'(k) + iG'(k)$, such that:

$$F'(k) = 1 - \frac{C_1 k^2}{(k^2 + C_2^2)},$$
$$G'(k) = -\frac{C_1 C_2 k}{(k^2 + C_2^2)},$$

k is the reduced frequency defined as:

$$k = \frac{c\omega}{2U}.$$

C_1 and C_2 are functions of the wing's aspect ratio AR such that:

$$C_1 = \frac{0.5AR}{2.32 + AR}, \tag{4.8}$$
$$C_2 = 0.181 + \frac{0.722}{AR}, \tag{4.9}$$

Due to the harmonic motion of flapping, the relative angle of attack is also periodic with the same frequency as flapping, such that:

$$\alpha = Ae^{i\omega t},$$
$$\dot{\alpha} = Ai\omega e^{i\omega t},$$
$$\dot{\alpha} = i\omega\alpha.$$

Substituting in equation 4.7, the flow's relative angle of attack is finally:

$$\alpha' = \frac{AR}{2 + AR}\left[F'(k)\alpha + \tfrac{c}{2U}\tfrac{G'(k)}{k}\dot{\alpha}\right] - \frac{w_0}{U}. \tag{4.10}$$

Finally, the downwash term is obtained from Kuethe and Chow (21) as:

$$\frac{w_0}{U} = \frac{2(\alpha_0 + \theta)}{2 + AR}, \tag{4.11}$$

where α_0 is the angle of the zero-lift line.

4.2 Dynamics

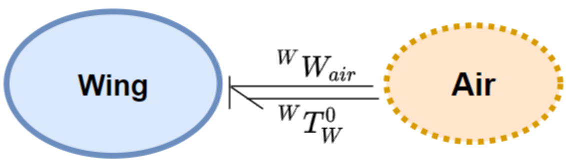

Figure 4.4: Aerodynamic contribution on the wing

This section derives the output wrench of the aerodynamic contribution on the wing. As shown in figure 4.4, the external port connected to the wing resembles these aerodynamic forces. This section answers the following question, given the ground Twist of the wing (${}^{W}\boldsymbol{T}_{W}^{0}$) as an input, what is the output aerodynamic forces (${}^{W}\boldsymbol{W}_{air}$) on each wing? It is worth noting that the aerodynamic forces are not only function of the twist of the wing. Other factors play a role in the generated forces such as the wind speed. As mentioned above, from strip theory, each strip is treated as a separate airfoil, thus each strip generates aerodynamic forces which is then transformed to the wing frame. Thus, the total aerodynamic contribution is the summation of the generated forces on each strip, all over the strips. Thus,

$$^{W}W_{air} = \sum_{j=1}^{N} {}^{W}W_{air,j} = \sum_{j=1}^{N} Ad^{\top}_{H_W^j}\, {}^{j}W_{air,j}, \tag{4.12}$$

where N is the total number of strips and j is the selected strip. The frame j is chosen such that its origin lies in the geometric center of each strip (half way chord-wise and width-wise). The $x-$ axis points forward, the $y-$ axis points to the left and the $z-$ axis points upwards.

For each strip, the generated aerodynamic forces can be divided into normal components that cause the lift and tangential components that cause thrust and drag, and a pitching moment. Thus, for each strip,

$$^{j}W_{air,j} = \begin{pmatrix} 0 \\ d\tau \\ 0 \\ dF_x \\ 0 \\ dN \end{pmatrix}, \tag{4.13}$$

where dF_x is the tangential forces along the chordwise direction, dN is the normal forces in the z direction, and $d\tau$ is the pitching moment. For the rest of the chapter, expressions for both the normal and tangential forces are derived. Since aerodynamic forces are function of the flow velocity around the wing, its worth mentioning different flow velocities at different locations first. These velocities will be used in the derivation of the generated forces.

4.2.1 Flow Velocities at different locations

Due to the unsteadiness of this aerodynamic model, aerodynamic forces occur at different chord-locations. So, in order to study the aerodynamic forces, flow velocities at different locations should be studied first. Figure 4.5 shows different velocity components of the flow around the wing.

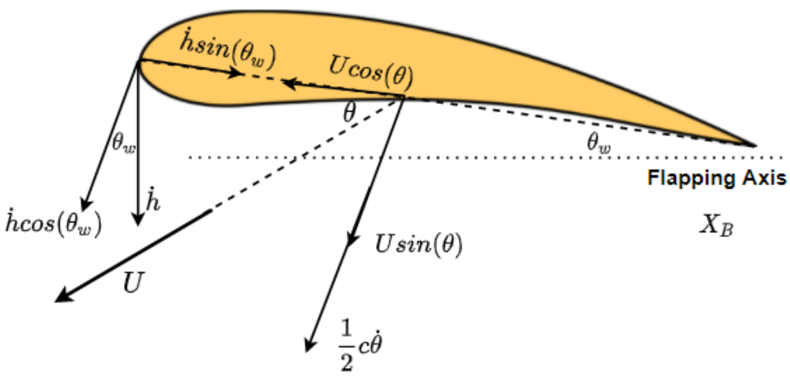

Figure 4.5: Flow velocities at different locations

Mid-chord Location

As mentioned before, three discrete motions play an important rule in wing's motion: forward, plunging and pitching.
Plunging motion ($\dot{\boldsymbol{h}}$) can be decomposed into two components: tangential component along the chord equals to $\dot{\boldsymbol{h}}\boldsymbol{sin}(\boldsymbol{\theta_w})$, and a normal component equals to $\dot{\boldsymbol{h}}\boldsymbol{cos}(\boldsymbol{\theta_w})$.

Similarly, forward motion $\boldsymbol{U}$ can be composed into a tangential term along the chord represented by $\boldsymbol{Ucos(\theta)}$ and a normal component equals to $\boldsymbol{Usin(\theta)}$.

Pitching has a normal component only equals to the radius of rotation ($\boldsymbol{\frac{1}{2}c}$) times the angular pitching velocity ($\boldsymbol{\dot{\theta}}$).

With that being said, tangential and normal flow velocities at mid-chord locations equal to:

$$V_x = Ucos(\theta) - \dot{h}sin(\theta_w), \tag{4.14}$$

$$V_n = Usin(\theta) + \dot{h}cos(\theta_w) + \frac{1}{2}c\dot{\theta}, \tag{4.15}$$

$$\hat{V} = \sqrt{V_x^2 + V_n^2}. \tag{4.16}$$

Quarter chord location

The tangential component is the same as the one mentioned above ($\boldsymbol{V_x}$). The normal component is slightly different, the flow velocity at $\frac{1}{4}$ chord location must include the downwash effect as well as the wing's motion relative to $\boldsymbol{U}$. The reason for that is the aerodynamic center is located at $\boldsymbol{\frac{1}{4}}$ chord location due to the airfoil being cambered.

$$\begin{aligned} V_x &= Ucos(\theta) - \dot{h}sin(\theta_w), \\ V_{nc} &= U(\alpha' + \theta) - \frac{1}{2}c\dot{\theta}, \\ V &= \sqrt{V_x^2 + V_{nc}^2}. \end{aligned} \tag{4.17}$$

After defining the kinematic model and flow velocities at different locations, we are ready to derive expressions for the generated aerodynamic forces. As mentioned earlier, there are two types of forces being generated. First, the normal forces which act normal to the chord of each airfoil section. Second, the tangential forces which act along the chord of each airfoil section. In the next two sections, expressions for the generated forces are given.

4.2.2 Normal Forces

Normal forces can be divided into two main components.

- Section's circulatory normal force at $\frac{1}{4}$ chord-location :

$$dN_c = \frac{\rho U V C_n(y)}{2} c dy, \tag{4.18}$$

  where $C_n(y) = 2\pi(\alpha' + \alpha_0 + \theta)$. For each airfoil section, dy is the width and c is the chord length. V is the flow velocity at $\frac{1}{4}$ chord location defined in equation 4.17.

- Apparent mass effect at $\frac{1}{2}$ chord:

$$dN_a = \frac{\rho\pi c^2}{4}\dot{v}_2 dy, \tag{4.19}$$

  where $\frac{\rho\pi c^2 dy}{4}$ is a virtual mass of air enclosed in a thin cylinder of width dy and diameter equals to section's chord length. $\dot{v}_2$ is the linarized time rate of the midchord normal velocity component, such that:

$$\dot{v}_2 = U\dot{\alpha} - \frac{1}{4}c\ddot{\theta}$$

- The final normal component is the summation of both terms:

$$dN = dN_c + dN_a. \tag{4.20}$$

4.2.3 Tangential Forces

- Garrick's expression for leading edge suction:

$$dT_s = \eta_s 2\pi(\alpha' + \theta - \frac{c\dot{\theta}}{4U})^2 \cdot \frac{\rho UV}{2} c dy, \tag{4.21}$$

where η_s accounts for partial edge suction.

- Chordwise friction drag due to viscosity:

$$dD_f = (C_d)_f \frac{\rho V_x^2}{2} c dy, \tag{4.22}$$

where V_x is the tangential velocity component defined in equation 4.14. $(C_d)_f$ is the drag coefficient due to skin friction, according to (16) it can be expressed as:

$$(C_d)_f = \frac{0.89}{[]log(Rn)]^{2.58}}.$$

- Chordwise friction due to camber:

$$dD_{camber} = -2\pi\alpha_0(\alpha' + \theta)\frac{\rho UV}{2} c dy \tag{4.23}$$

- Final Tangential force is then:

$$dF_x = dT_s - dD_f - dD_{camber}. \tag{4.24}$$

So far in this chapter, final expressions for the generated forces are defined. In the next section, it is shown how this aerodynamic model accounts for post-stall behaviour.

4.2.4 Post-stall behaviour

So far, the derived expressions were for attached flow when the relative angle of attack is within the allowed range, in other words, when it is smaller than the max stall angle. When the angle exceeds the stall angle, the flow is assumed to be totally separated and that implies that chordwise forces vanish. The section's circulatory normal force tend to be:

$$(dN_c)_{sep} = (C_d)_{cf} \frac{\rho \hat{V} V_n}{2} c dy, \tag{4.25}$$

where $\hat{V}$ is the flow velocity at mid-chord location and V_n is its normal component defined in equations 4.16 and 4.15, respectively. $(C_d)_{cf}$s is the post-stall normal force coefficient chosen to be 1.98 according to (16).
The normal force due to the apparent mass effects is assumed to be half that of attached flow:

$$(dN_a)_{sep} = \frac{1}{2} dN_a. \tag{4.26}$$

To check for post stall behaviour, according to (26):

if $\quad (\alpha_{stall})_{min} \leq \left[\alpha' + \theta - \frac{3}{4}\frac{c\dot{\theta}}{U}\right] \leq (\alpha_{stall})_{max} \quad$ **then**

$$dF_x = dT_s - dD_f - dD_{camber}, \tag{4.27}$$

$$dN = dN_c + dN_a. \tag{4.28}$$

else

$$dF_x = 0, \tag{4.29}$$

$$dN = (dN_c)_{sep} + (dN_a)_{sep}. \tag{4.30}$$

end if

4.2.5 Wrench Output

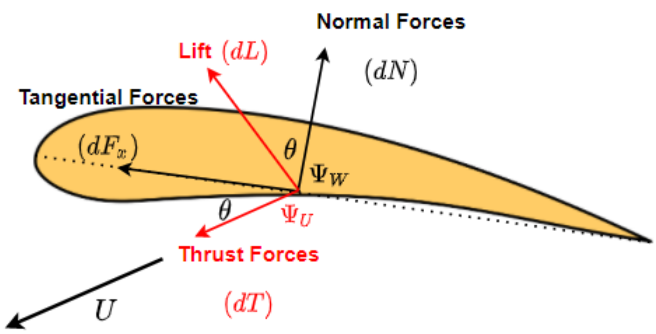

Figure 4.6: Wrench transformation from the wing frame Ψ_W to the flight direction frame Ψ_U

The tangential and normal forces expressed in the wing frame are then transformed to the frame $\boldsymbol{\Psi_U}$ such that the *x-axis* of $\boldsymbol{\Psi_U}$ aligns with the flight direction $\boldsymbol{U}$ and the *z-axis* is pointed upwards normal to the flight direction, as shown in figure 4.6. The transformation is then:

$$\begin{pmatrix} {}^U dL \\ {}^U dT \end{pmatrix} = \begin{pmatrix} cos(\theta) & sin(\theta) \\ -sin(\theta) & cos(\theta) \end{pmatrix} \begin{pmatrix} {}^W dN \\ {}^W dF_x \end{pmatrix} \tag{4.31}$$

Since each wing is divided into strips along its span, The final lift and thrust forces are then calculated as the summation of all forces in each strip:

$$L = 2\sum_i dL_I cos(\gamma) \tag{4.32}$$

$$T = 2\sum_i dT_i \tag{4.33}$$

The lift force is resolved into two components, upward lift represented by $\boldsymbol{Lcos(\gamma)}$ and sideway forces expressed by $\boldsymbol{Lsin(\gamma)}$. In case of symmetric flapping, the side forces from both wings cancel each other, thats why the term does not appear in the equations. Finally, both the lift and thrust are doubled to account for the two wings.

4.3 Conclusion

Following the dynamic model of a flapping-wing UAV presented in the previous chapter, this chapter completes the model by defining the aerodynamic forces on the wing. The aerodynamic model adopted here is the same model of Delaurier (8). The model accounts for most of the unsteady phenomenon of flapping flight such as vortex wake, apparent mass effect and partial edge suction by means of modified strip theory. The chapter starts with defining the kinematics of flapping flight, followed by a brief discussion of different angles made by the airfoil. Moreover, a detailed derivation of the generated normal and tangential forces was discussed. Forces are then transformed into the wing frame to be consistent with the modeling strategy used in this thesis. In the next chapter, the aerodynamic model is validated through a set of experiments including time response and sweep over different parameters.

5 Experiments and Results

This chapter validates the aerodynamic model adopted in the previous chapter. Through a set of experiments, the behaviour of the aerodynamic model is observed and studied. Experiments simulate the Robird being in a **wind tunnel**. To do so, the base body is being fixed and the speed of the bird is determined by the speed of the wing facing it. By setting the velocity of the base-body to zero, its guaranteed to be fixed. Thanks to the port-based approach and bond graph, this can be done easily by using a zero source of flow **Sf** connected to the base-body Twist.

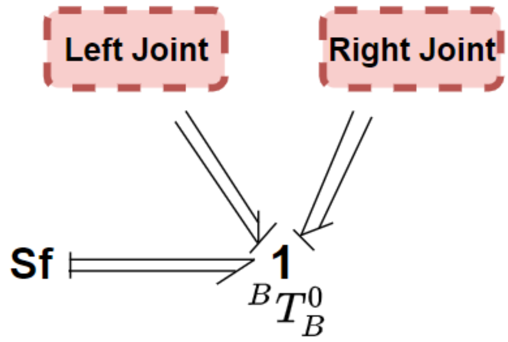

Figure 5.1: Base-body velocity is fixed to zero to simulate the bird being in a wind tunnel.

5.1 Test Wing

For validation of the aerodynamic model explained earlier, a test wing is used. The wing has the dimensions and characteristics of the Robird's wing, but with a different airfoil. The airfoil used for these simulations is the **Liebeck LPT 110A**. To perform these experiments on the Robird's wing, these values have to be changed according to the airfoil of the Robird: Angle of section's zero-lift line $\boldsymbol{\alpha_0}$, Leading edge suction efficiency $\boldsymbol{\eta_s}$ and maximum stall angle $\boldsymbol{(\alpha_{stall})_{max}}$

5.2 Chapter Outline

The chapter is organised as follows, four experiments are being conducted. In each section, the experiment setup is explained, including different parameters being used. For example, wind speed ($\boldsymbol{U(m/sec)}$), pitch angles ($\boldsymbol{\theta_a}, \boldsymbol{\theta_w}(°)$) and flapping frequency ($\boldsymbol{f(Hz)}$). Later, the results of each experiment are shown and discussed. Based on each experiment's results, the next experiment setup is decided. For the results, graphs of **Tangential, Normal, Lift** and **Thrust forces** are shown, as well as the **Effective angle of attack** ($\boldsymbol{\alpha'}(°)$). To avoid confusion between the four forces, figure 5.2 show the two frames $\boldsymbol{\Psi_W, \Psi_U}$ where the forces are expressed in. Normal and Tangential forces are expressed in the wing frame $\boldsymbol{\Psi_W}$ whereas lift and thrust are expressed in the flight direction frame $\boldsymbol{\Psi_U}$. Before starting the experiments, some parameters are fixed for all experiments. These parameters depend on the characteristics of the airfoil and the Robird (11). The following table summarizes these parameters.

W	b	AR	Γ	α_0	η_s	$(\alpha_{stall})_{max}$
$0.73Kg$	$1.12m$	8.651	20°	0.5°	0.98	13°

Last but not least, the first experiment is a time response of the aerodynamic model where the generated aerodynamic forces are shown with standard flight parameters. For the rest of experiments, a sweep over different parameters is carried out to see the effect of the chosen

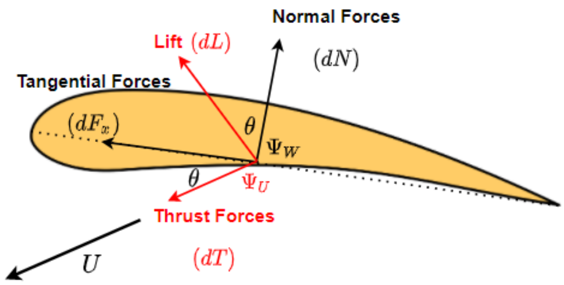

Figure 5.2: An airfoil section showing the two different frames $\boldsymbol{\Psi_W, \Psi_U}$ forces are expressed in

parameter on the generated output. For each experiment, the average of the generated forces are plotted for each value of the chosen parameter. The average (for the lift for example) is calculated as follows:

$$L = \frac{1}{T}\int_0^T L(\tau)\,d\tau, \tag{5.1}$$

where T is the time period of a flapping cycle. Finally, as mentioned earlier, 4 generated forces are shown in each experiment. Figure 5.3 shows the four generated forces, with the chosen force highlighted in green to make it easier for the reader to follow.

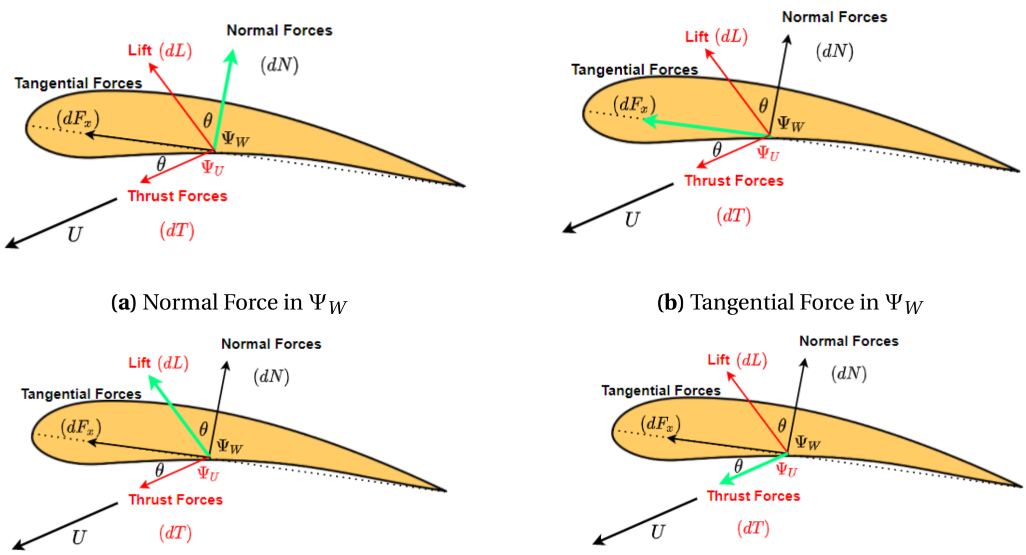

(a) Normal Force in Ψ_W

(b) Tangential Force in Ψ_W

(c) Lift in Ψ_U

(d) Thrust in Ψ_U

Figure 5.3: Generated Aerodynamic forces with the chosen force highlighted in green ((a) Normal Force, (b) Tangential Force, (c) Lift, (d) Thrust)

5.3 Experiment 1: Time History of the Aerodynamic model

5.3.1 Experiment Setup

The first experiment validates the model using the same parameters that were used in one of the first papers introducing the Robird (11). Flight speed of $\boldsymbol{U = 10 m/sec}$, pitch angle $\boldsymbol{\theta_a = 7.5°}$ and flapping frequency chosen to be $\boldsymbol{f = 1.2Hz}$. One of the first aims of this experiments is to check the periodic behaviour of the wings' motion. Furthermore, the average generated lift should have a positive value to ensure that the Robird can fly.

5.3.2 Results

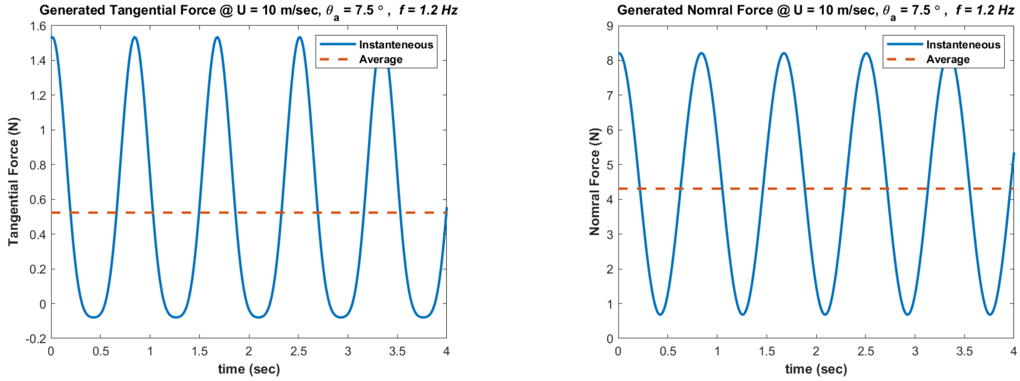

Figure 5.4: Tangential and Normal forces expressed in the wing frame $\boldsymbol{\Psi_W}$ resulting from Experiment 1

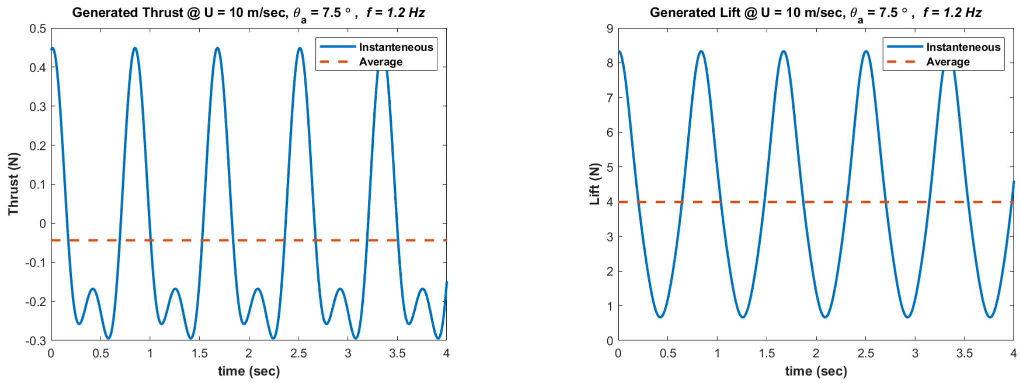

Figure 5.5: Generated Thrust and lift expressed in the flight direction frame $\boldsymbol{\Psi_U}$

Figure 5.4 shows the tangential and normal forces, $\boldsymbol{dF_x, dN}$, respectively. As it can be seen here, the periodic behaviour of the generated forces is confirmed. Furthermore, the forces are periodic with the same frequency as flapping $\boldsymbol{f = 1.2Hz}$. Moreover, both forces have a positive valued average which indicates that each airfoil section is capable of generating positive thrust and lift.

After doing the wrench transformation from the wing frame $\boldsymbol{\Psi_W}$ to the flight direction's frame $\boldsymbol{\Psi_U}$, the generated lift and thrust are shown in figure 5.5. Again, the lift has a positive average with a realistic value of **4 N**. It is to be noted that these are the forces generated from one wing. Total generated lift from the two wings will then be **8 N**. Noting that the mass of the Robird is **0.73 Kg**, the required lift overcome the Robird's weight is **7.1613 N**. Which means that the generated lift is higher than the Robird's weight which validates the model in this aspect. On the other hand, the generated thrust force has a negative valued average which implies that the drag and friction forces are more than the forward force. This could be due to many reasons. For example, the flight speed maybe not large enough to cause the Robird to generate a thrust and move forward. Same applies to the pitch angle and the flapping frequency. With that being said, in the next experiments, a sweep over these parameters is performed to reach the best configuration which causes the bird to fly. Finally, the effective angle of attack $\boldsymbol{\alpha'}$ is shown in figure 5.5. it can be confirmed that it has a periodic behaviour with the same frequency of flapping. Moreover, it can be seen here that the effective angle of attack $\boldsymbol{\alpha'}$ does not exceed the stall angle $\boldsymbol{(\alpha_{stall})_{max} = 13°}$ and stays in the range of $[-7°, 4°]$.

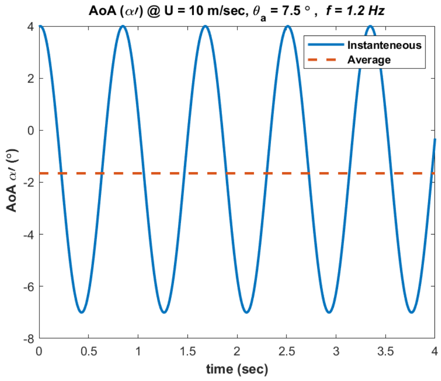

Figure 5.6: The effective angle of attack $\boldsymbol{\alpha'}$ resulting from the first experiment

5.4 Experiment 2: Effect of the pitch angle θ_a on the Aerodynamic behaviour

5.4.1 Experiment Setup

In this experiment, the pitch angle $\boldsymbol{\theta_a}$ is the variable of interest. The aim of this experiment is to see how the pitch angle affects the behaviour of the generated forces and the angle of attack. This is done through a sweep over the pitch angle θ_a in the range of $[-20°, 20°]$. The other flight parameters including flight speed and the flapping frequency are kept the same as the last experiment. $\boldsymbol{U = 10 m/sec, f = 1.2Hz}$

5.4.2 Results

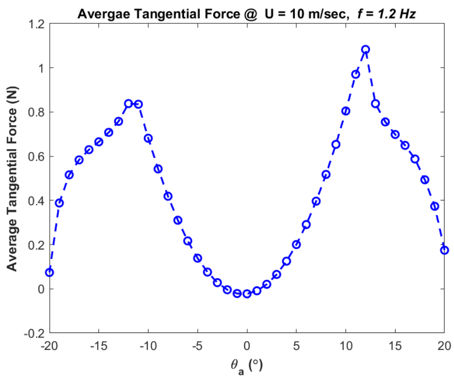

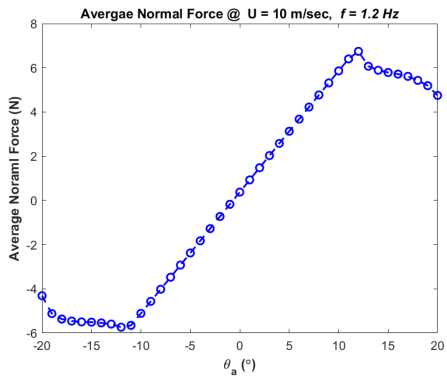

Figure 5.7: Tangential and Normal forces expressed in the wing frame $\boldsymbol{\Psi_W}$ resulting from Experiment 2

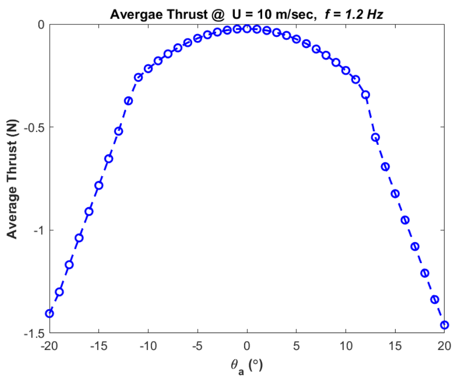

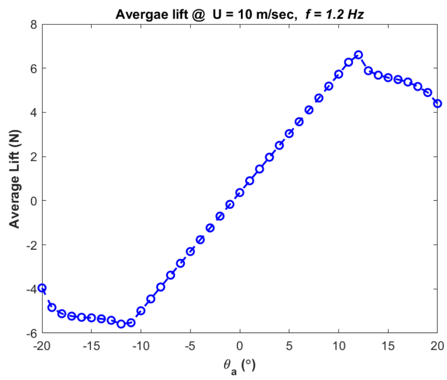

Figure 5.8: Generated Thrust and lift expressed in the flight direction frame $\boldsymbol{\Psi_U}$

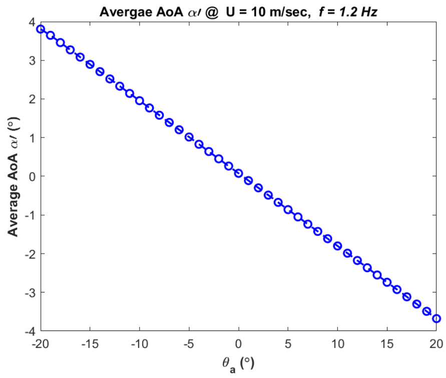

Figure 5.9: The effective angle of attack $\boldsymbol{\alpha'}$ resulting from the second experiment showing a linear function of the pitch angle $\boldsymbol{\theta_a}$

This experiment showed very informative results about the behaviour of generated forces. In figure 5.7, it can be seen that both the normal and tangential forces follow the same aerodynamic behaviour of lift and drag coefficients, respectively versus the angle of attack. For the normal forces, it has a linear function of the pitch angle until a certain pitch angle then the magnitude starts decreasing due to stall effect. Also, for a negative pitch angle, the magnitude has a negative value implying negative lift. In figure 5.8, the lift has a similar behaviour as well. Moreover, it can be seen that at zero pitch angle, there is a very small value of lift around **0.5°**, which is exactly the same value of zero-lift line used in the model $\boldsymbol{\alpha_0}$.
For the tangential forces in figure 5.7, magnitude starts to increase until the stall angle and starts to decrease again. Moreover, the magnitude is positive even for negative pitch angles which makes sense, since the orientation of pitching does not affect the forces in the **x-axis** of $\boldsymbol{\Psi_W}$. Still the thrust graph has negative values for every pitch angle. So, this gives an indication that there is no influence from the pitch angle on the sign of thrust forces (expressed in $\boldsymbol{\Psi_U}$) being generated.
Finally, one interesting result is the linear relation between the effective angle of attack $\boldsymbol{\alpha'}$ and the pitch angle $\boldsymbol{\theta_a}$. The negative relation can be verified from equation 4.7.

5.5 Experiment 3: Effect of flight speed U on the Aerodynamic behaviour

5.5.1 Experiment Setup

In this experiment a sweep over the flight speed **U (m/sec)** is performed. Same as the last experiment,the objective of this experiment to see the effect of the flight speed on the generated forces and the effective angle of attack of the system. Other flight parameters are kept the same $\boldsymbol{\theta_a = 7.5°}$, $\boldsymbol{f = 1.2Hz}$

5.5.2 Results

This experiments tests the effects of flight speed **U** on the behaviour of the aerodynamic model. As figures 5.10, 5.11 show, there is a direct relation between the flight speed and the generated forces. As the flight speed increases, the magnitude of the generated forces increase as well. It was also seen that the magnitude of the thrust increases but in the negative direction, so again, flight speed has no influence on the sign of the thrust. In the next experiment, the flapping frequency is being swept over hoping that it will give an indication about the sign of the thrust forces. Finally, the average of the effective angle of attack is plotted in figure 5.12. There is a slight increase in the magnitude of the angle of attack, in the order of magnitude of **0.1°**.

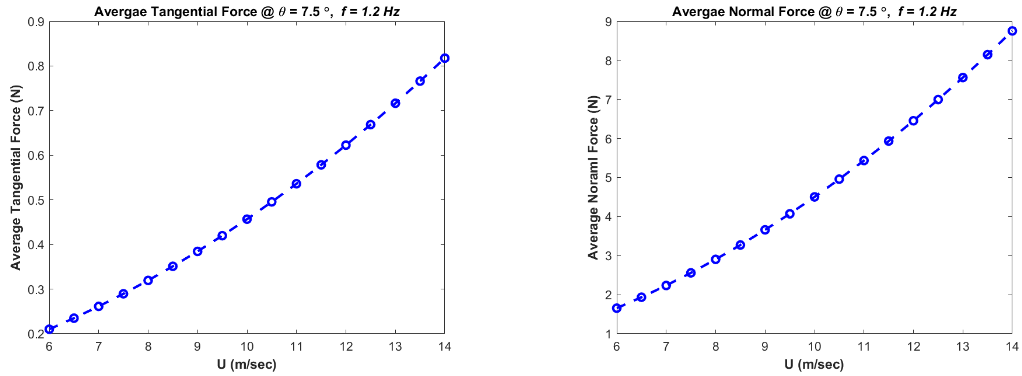

Figure 5.10: Tangential and Normal forces expressed in the wing frame $\boldsymbol{\Psi_W}$ resulting from Experiment 3 show a direct relation with the flight speed

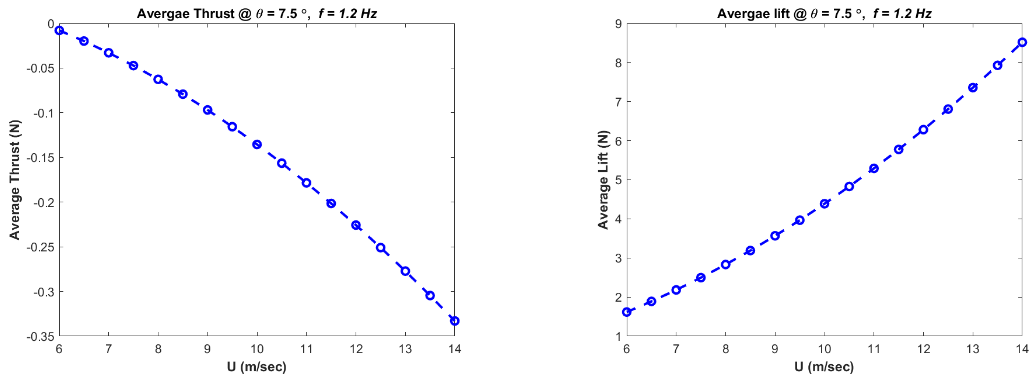

Figure 5.11: Generated Thrust and lift expressed in the flight direction frame $\boldsymbol{\Psi_U}$

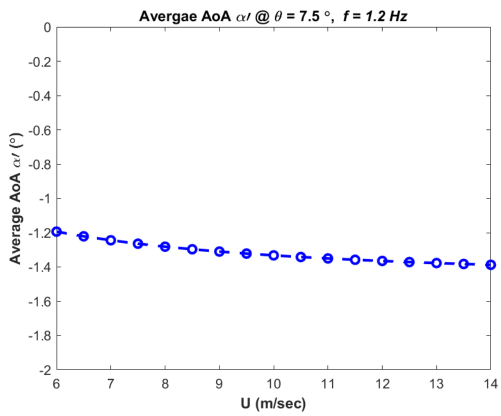

Figure 5.12: Slight decrease in the effective angle of attack $\boldsymbol{\alpha'}$ with the change of the flight speed $\boldsymbol{U}$

5.6 Experiment 4: Effect of flapping frequency f on the Aerodynamic behaviour

5.6.1 Experiment Setup

So far, the results of the previous experiments validate some aspects of the aerodynamic model being adopted. However, the reason for negative thrust being generated is still not known. In this experiment, the flapping frequency is being swept over hoping to give a clue about the negative thrust. Flight speed is chosen to be $\boldsymbol{U = 10 m/sec}$ along with a pitch angle $\boldsymbol{\theta_a = 7.5°}$.

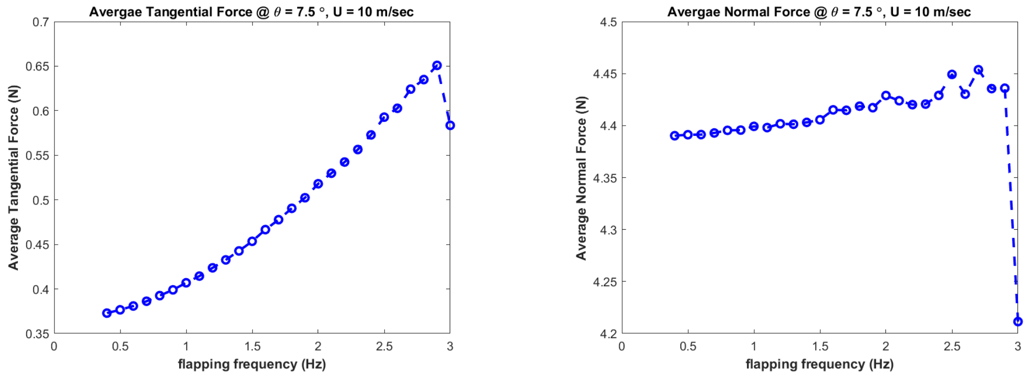

Figure 5.13: Tangential and Normal forces expressed in the wing frame $\boldsymbol{\Psi_W}$ resulting from Experiment 4

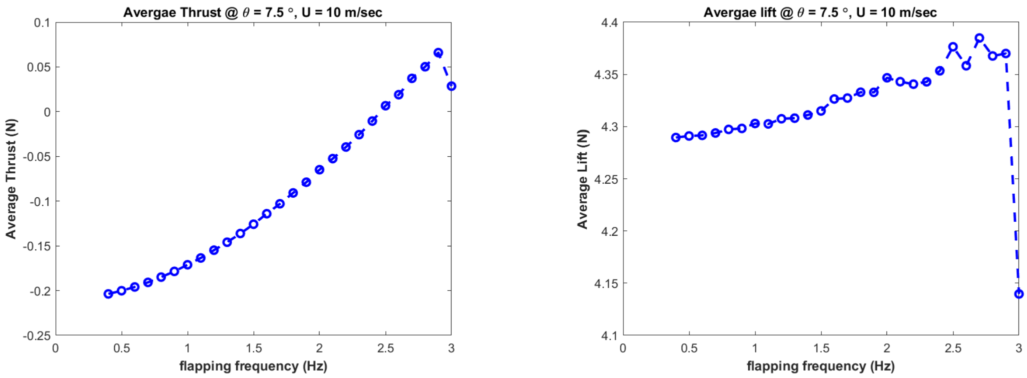

Figure 5.14: Generated Thrust and lift expressed in the flight direction frame $\boldsymbol{\Psi_U}$

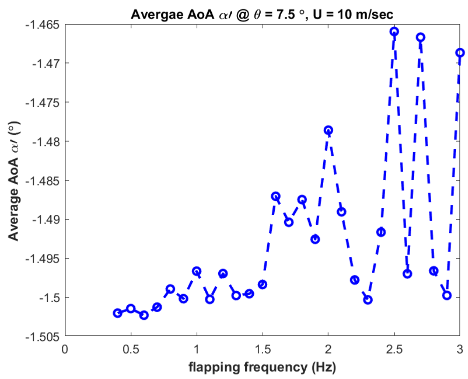

Figure 5.15: Slight decrease in the effective angle of attack $\boldsymbol{\alpha'}$ with the change of the flight speed $\boldsymbol{U}$

5.6.2 Results

Figures 5.13, 5.14 show the behaviour of the generated forces with different flapping frequencies. Results of this experiment explain why the thrust used to have negative values for all the previous experiments. The thrust in figure 5.14 is shown to be negative as long as the flapping frequency is less than 2.5. It is also shown that the maximum value of thrust is achieved when the flapping frequency is around 2.9 Hz. That is quite impressive since this result agree with the same flapping frequency used in the work of (12) where they were studying the wake effects present in the Robird in wind tunnel experiments. The experiment showed that the average lift keeps increasing with the increase of flapping frequencies, except for the last frequencies of 2.5

to 3 Hz, where it exhibited some oscillations within a small order of magnitude. Finally, It is shown that the effective angle of attack keeps changing within a small order of magnitude.

5.7 Conclusion

In this chapter, 4 experiments were carried out to validate the Aerodynamic model adopted in this work. In the first experiment, the model was proven to output an average positive valued lift which implies that the bird can overcome its weight and go up. There was a problem with the generated thrust as it had a negative average which means that the drag forces were higher than the forward thrust.

In the second experiment, a sweep over different pitch angles $\boldsymbol{\theta_a}$ is done. That confirmed the aerodynamic behaviour of the generated forces, in the sense of $\boldsymbol{C_l, C_D}$ vs the angle of attack $\boldsymbol{\alpha'}$. This is shown in the graphs of the lift and drag forces versus the pitch angle of the bird. Moreover, the post stall behaviour is seen to be accounted for. One last interesting observation, the effective angle of attack $\boldsymbol{\alpha'}$ seems to have a linear relationship with the pitch angle of the bird. Still, the second experiment was not able to answer any questions regarding the negative thrust values.

In the third experiment, the generated forces were plotted versus different flight speeds $\boldsymbol{U}$. This experiment confirmed the direct relation between flight speed and the magnitude of the generated forces. The more the flight speed is, the greater the magnitude of the generated lift and thrust. Still, the thrust was increasing but in the negative direction.

Finally, the last experiment investigated the effect of different flapping frequencies on the system behaviour. It was seen that for a specific range of flapping frequencies (2.5 to 3 Hz), the thrust tend to be positive. This explains why in the first three experiments, there were always negative thrust generated. Although the wing used for these experiments is different than the wing of the Robird due to difference in the airfoil along the span, an optimal flapping frequency of 2.9 Hz which maximizes the thrust and generates positive lift, matches a previous work done on the Robird in a wind tunnel by (12).

6 Conclusion and Future Work

6.1 Conclusion

This research started with the following research questions:

How can a port-based modeling approach be used to model an ornithopter like the Robird? Moreover, how can the Port-Hamiltonian framework play its rule in them odeling process?

In the third chapter, a dynamic model for flapping-wing UAVs was developed in the port Hamiltonian framework. The full model is seen as an interconnection between different sub-systems which are exchanging energy. These sub-systems are the base body, two wings, two joints and the aerodynamic contribution on the wings. Skew-symmetric Dirac structures for each interconnection were derived, thus, preserving the power balance of the system. Furthermore, the port Hamiltonian model is an open model which allows for interaction with external ports such as the environment or a controller sub-system. The dynamic model fits in place with the aerodynamic part, since it can be seen as an exchange of energy between the flapping wing and the air flow around it. With this being said, a full dynamic model of flapping wing UAVs was derived in an energy-based manner.

The second research question was:

How can the aerodynamics of ornithopters be modeled without assuming quasi-steady assumptions? Can we reach a strong model that captures unsteady phenomenon of flight and validate this model on the Robird?

In the fourth chapter, an unsteady aerodynamic model which accounts for most of the unsteady phenomenon of flapping flight was adopted. The model takes into account unsteady vortex wake through modified strip theory. Moreover, it takes into consideration, unsteady phenomenon such as apparent mass effect, camber partial edge suction, down-wash effect and viscosity of the flow. In addition, the model accounts for post stall behaviour. The model was validated through a set of 4 experiments which predict its behaviour. Experiments showed that the adopted aerodynamic model predicts positive generated lift with a an average higher than the weight of the Robird. Moreover, in the second experiment, the aerodynamic behaviour of the generated normal and tangential forces was observed. With small pitch angles, lift varies linearly with the pitch angle until it reaches the stall angle then it starts to go down. The third experiment confirmed the effect of flight speed on the generated forces. The higher the speed is, the larger the magnitude of the generated forces. Finally, the fourth experiment showed an optimal value of flapping frequency of 2.9 Hz that maximizes the lift and generates positive thrust. This value agrees with the work of (12), which was done on the Robird. It is worth emphasising that the wing used for the experiments is different than the Robird's wing due to the difference in the airfoil along the span. However, they are similar in the dimensions and other flight parameters.

In conclusion, this work provides a full dynamic model of flapping-wing UAVs with an unsteady, realistic aerodynamic model which does not assume quasi-steady assumptions. The aerodynamic model was proven to work through a set of experiments which validated its behaviour.

6.2 Future Work

The presented work in this thesis can be extended in many ways:

- The preliminary dynamic model treated the flapping-wing UAV as a base body connected to two wings. The tail was neglected but can be easily included as an added sub-system. Further more, aerodynamic contribution on the base body was neglected, and this can be easily added through connecting an external power port to the base body. Thanks to the port based modeling technique adopted, these external sub-systems can be easily connected without the need to change the rest of the model. Thus providing a more realistic model.

- On having a full model of the flapping-wing UAV, the next step is to design the controller and connecting it as a sub-system. Control by interconnection is then the perfect candidate approach for controller design along with damping injection and energy shaping.

- Simulations made in the last chapter treated the wing as one plate with an airfoil section. In other words, the wing was seen as only one strip. Although results validated the aerodynamic model used, a more realistic model is achieved by increasing the number of strips as seen in figure 6.1.

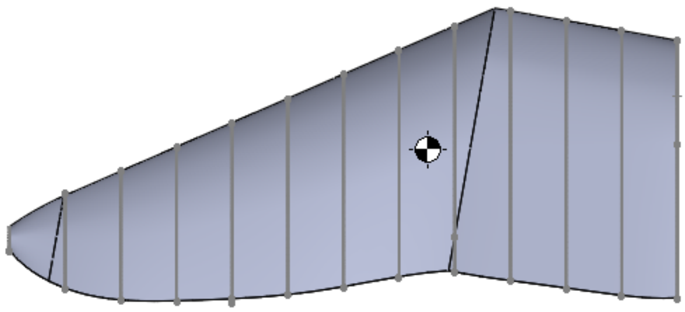

Figure 6.1: The Robird's wing is divided into 12 equal strips

- Finally, experiments conducted in this thesis validated the aerodynamic model, but they did not simulate flight behaviour. Given the full Port Hamiltonian model derived in this thesis, flight experiments can be conducted after designing the controller.

Bibliography

[1] Ali R Ahmadi and Sheila E Widnall. Energetics and optimum motion of oscillating lifting surfaces of finite span. *Journal of Fluid Mechanics*, 162:261–282, 1986.

[2] John David Anderson Jr. *Fundamentals of aerodynamics*. Tata McGraw-Hill Education, 2001.

[3] Akira Azuma, Soichi Azuma, Isao Watanabe, and Toyohiko Furuta. Flight mechanics of a dragonfly. *Journal of experimental biology*, 116(1):79–107, 1985.

[4] Akira Azuma and Tadaaki Watanabe. Flight performance of a dragonfly. *Journal of Experimental Biology*, 137(1):221–252, 1988.

[5] Moble Benedict, K Sudhakar, and K Kurien Issac. Aeroelastic design and manufacture of an efficient ornithopter wing. *Department of Aerospace Engineering, Indian Institute of Technology, Bombay, Mumbai*, 2004.

[6] DS Betteridge and RD Archer. A study of the mechanics of flapping wings. *Aeronautical Quarterly*, 25(2):129–142, 1974.

[7] Peter C Breedveld. Port-based modeling of mechatronic systems. *Mathematics and Computers in Simulation*, 66(2-3):99–128, 2004.

[8] James D DeLaurier. An aerodynamic model for flapping-wing flight. *The Aeronautical Journal*, 97(964):125–130, 1993.

[9] Harijono Djojodihardjo, Alif Syamim Syazwan Ramli, and Surjatin Wiriadidjaja. Kinematic and aerodynamic modelling of flapping wing ornithopter. *Procedia Engineering*, 50(9):848–863, 2012.

[10] CP Ellington. Vortices and hovering flight. *Instationäre Effekte an Schwingenden Tierflügeln*, pages 64–101, 1980.

[11] Gerrit Adriaan Folkertsma, Wessel Straatman, Nico Nijenhuis, Cornelis Henricus Venner, and Stefano Stramigioli. Robird: a robotic bird of prey. *IEEE robotics & automation magazine*, 24(3):22–29, 2017.

[12] Luuk Groot Koerkamp, Leandro D de Santana, Harry W Hoeijmakers, and Kees H Venner. Investigation into wake of flapping wing of robotic bird. In *AIAA Aviation 2019 Forum*, page 3582, 2019.

[13] Jean-Luc Guermond and Antoine Sellier. A unified unsteady lifting-line theory. *Journal of Fluid Mechanics*, 229:427–451, 1991.

[14] Robyn Lynn Harmon. *Aerodynamic modeling of a flapping membrane wing using motion tracking experiments*. PhD thesis, 2008.

[15] Mostafa Hassanalian and Abdessattar Abdelkefi. Classifications, applications, and design challenges of drones: A review. *Progress in Aerospace Sciences*, 91:99–131, 2017.

[16] Sighard F Hoerner. Fluid-dynamic drag. *Hoerner fluid dynamics*, 1965.

[17] Darryl D Holm, Jerrold E Marsden, and Tudor S Ratiu. The euler–poincaré equations and semidirect products with applications to continuum theories. *Advances in Mathematics*, 137(1):1–81, 1998.

[18] Robert T Jones. *The unsteady lift of a wing of finite aspect ratio*, volume 681. NACA, 1940.

[19] Ramji Kamakoti, Mats Berg, Daniel Ljungqvist, and Wei Shyy. A computational study for biological flapping wing flight. , 32(4):265–279, 2000.

[20] Keiji Kawachi. *An Extention of the Local Momentum Theory to a Distorted Wake Model of a Hovering Rotor*. NASA, 1981.

[21] Arnold M Kuethe. Foundations of aerodynamics: bases of aerodynamic design. *University of Michigan, USA, John Wiley & Sons, New York, Printed in the USA, ISBN: 0-471-50953-1*, 1976.

[22] CE Lan. The unsteady quasi-vortex-lattice method with applications to animal propulsion. *Journal of Fluid Mechanics*, 93(4):747–765, 1979.

[23] Pengzhi Lin. *Numerical modeling of water waves*. CRC Press, 2008.

[24] H. Paynter. Analysis and design of engineering system. 01 1961.

[25] PJ Phlips, RA East, and NH Pratt. An unsteady lifting line theory of flapping wings with application to the forward flight of birds. *Journal of fluid mechanics*, 112:97–125, 1981.

[26] Raymond W Prouty. *Helicopter performance, stability, and control*. 1995.

[27] Ramy R Rashad. Energy-based modeling and control of interactive aerial robots: A geometric port-hamiltonian approach. 2021.

[28] J Mo V Rayner. A vortex theory of animal flight. part 1. the vortex wake of a hovering animal. *Journal of Fluid Mechanics*, 91(4):697–730, 1979.

[29] J Mo V Rayner. A vortex theory of animal flight. part 2. the forward flight of birds. *Journal of Fluid Mechanics*, 91(4):731–763, 1979.

[30] J Otto Scherer. Experimental and theoretical investigation of large amplitude oscillation foil propulsion systems. Technical report, HYDRONAUTICS INC LAUREL MD, 1968.

[31] M Smith, P Wilkin, and M Williams. The advantages of an unsteady panel method in modelling the aerodynamic forces on rigid flapping wings. *Journal of Experimental Biology*, 199(5):1073–1083, 1996.

[32] GR Spedding. The aerodynamics of flight. *Advances in comparative and environmental physiology*, 11:51–111, 1992.

[33] Stefano Stramigioli and Herman Bruyninckx. Geometry and screw theory for robotics. *Tutorial during ICRA*, 2001:75, 2001.

[34] Shigeru Sunada, Keiji Kawachi, Isao Watanabe, and Akira Azuma. Fundamental analysis of three-dimensional 'near fling'. *Journal of Experimental Biology*, 183(1):217–248, 1993.

[35] Shigeru Sunada, Keiji Kawachi, Isao Watanabe, and Akira Azuma. Performance of a butterfly in take-off flight. *Journal of Experimental Biology*, 183(1):249–277, 1993.

[36] Haithem E Taha, Muhammad R Hajj, and Ali H Nayfeh. Flight dynamics and control of flapping-wing mavs: a review. *Nonlinear Dynamics*, 70(2):907–939, 2012.

[37] Dragos Viieru. *Flapping and fixed wing aerodynamics of low Reynolds number flight vehicles*. University of Florida, 2006.

[38] Mohamed Y Zakaria, Haithem E Taha, and Muhammad R Hajj. Design optimization of flapping ornithopters: the pterosaur replica in forward flight. *Journal of Aircraft*, 53(1):48–59, 2016.

[39] MY Zakaria, AM Elshabka, AM Bayoumy, and OE Abd Elhamid. Numerical aerodynamic characteristics of flapping wings. In *International Conference on Aerospace Sciences and Aviation Technology*, volume 13, pages 1–15. The Military Technical College, 2009.